Reaction of Cl with vibrationally excited CH_4 and CHD_3: State-to-state differential cross sections and steric effects for the HCl product

William R. Simpson, T. Peter Rakitzis, S. Alex Kandel, Andrew J. Orr-Ewing,[a)]
and Richard N. Zare
Department of Chemistry, Stanford University, Stanford, California 94305

(Received 28 April 1995; accepted 26 July 1995)

The mechanism for the reaction of atomic chlorine with vibrationally excited methane is investigated by measurement of correlated state and scattering distributions using the method of core extraction (see preceding paper). Laser photolysis of molecular chlorine creates monoenergetic chlorine atoms (>98% Cl $^2P_{3/2}$) that react with vibrationally excited methane molecules prepared by linearly polarized infrared laser excitation. The resulting HCl product population distributions are determined by (2+1) resonance-enhanced multiphoton ionization (REMPI), and the differential cross section for each product rovibrational state is measured by core extraction. Approximately 30% of the product is formed in HCl($v=1,J$) with a cold rotational distribution; the remaining population is formed in HCl($v=0,J$) and is more rotationally excited. We observe a rich variation of the scattered flux that is dependent on the internal-energy state of the product. The HCl($v=1$) product is sharply forward scattered for low J and becomes nearly equally forward–backward scattered for high J; the HCl($v=0,J$) product is back and side scattered. The reactions of Cl with C–H stretch-excited methane (CH_4) and C–H stretch-excited CHD_3 are found to have similar angular and internal-state distributions. Observation of the spatial anisotropy of the HCl($v=0$, $J=3$) product shows that significant vibrational excitation of the methyl fragment does not occur. The measured spatial anisotropy is most consistent with a model in which backscattered HCl($v=0$, $J=3$) is formed in coincidence with slight methyl vibrational excitation and the forward-scattered HCl($v=0$, $J=3$) is formed in coincidence with no methyl excitation. The approach of the attacking chlorine atom with respect to the C–H stretch direction can be varied by rotating the plane of polarization of the infrared excitation. A marked steric effect is observed in which Cl atoms approaching perpendicular to the C–H stretch preferentially yield forward-scattered HCl($v=1$) product. On the other hand, the reaction is weakly dependent on the rotational quantum state of $CH_4(v_3=1,J)$, and on the rotational polarization. The data are consistent with a model that has a widely open ''cone of acceptance'' in which the impact parameter controls the internal-state and scattering distributions of the HCl product. © *1995 American Institute of Physics.*

I. INTRODUCTION

Hydrogen-atom abstraction reactions represent an important proving ground for chemical reaction dynamics.[1] These light atom transfer reactions are theoretically tractable in full quantum mechanical calculations, and their products are spectroscopically convenient for state-resolved experimental studies. In the past, experimental techniques have allowed the measurement of scattering distributions and product rovibrational population distributions but seldom both in coincidence.[2] The technique of core extraction, described in the previous paper, provides a method to make this coincident measurement of internal-state and angular-scattering distributions. Our long-standing interest in the effects of vibrational excitation on chemical reactions has led us to apply this technique to the reaction $Cl(^2P_{3/2})+CH_4(v_3=1,J)\rightarrow HCl(v,J)+CH_3$ and its isotopically related cousin $Cl(^2P_{3/2})+CHD_3(v_1=1,J)\rightarrow HCl(v,J)+CD_3$.

Vibrational excitation of reagents in hydrogen-atom abstraction reactions has shown many interesting results. The most obvious such result is enhancement of the reaction cross section, which has been observed in many cases, the simplest of which is the $D+H_2$ reaction.[3,4] For polyatomic reaction systems, energy can be localized to some part of the reagent, which has been shown in many cases to lead to control of subsequent chemical branching between products. This effect, known as mode- or bond-selective chemistry, has been observed in a growing number of systems.[5–8] This study attempts to understand these vibrational effects by observing correlated internal-state and angular-scattering distributions in one such vibrationally excited reaction.

Although the reaction of atomic chlorine with methane has received only limited experimental and theoretical attention,[9–13] the related reactions of O(^3P) with hydrocarbons provide insight into our reaction system. In a mechanistic study of the reactions of atomic oxygen (^3P) with hydrocarbons, Luntz and Andresen[14,15] measured rovibrational state distributions for the OH product as a function of both collision energy and nature of hydrocarbon reagent. They found rotationally cold population distributions with vibrational distributions that became more excited as the site of hydrogen-atom abstraction varied from primary through tertiary. In their quasiclassical trajectory calculations for these reactions,[15] they found that the cold rotational distributions were associated with backscattered, rebound trajecto-

[a)]Present address: School of Chemistry, University of Bristol, BS8 1 TS, U.K.

ries, which made an important link between scattering and rotational state distributions. Since this seminal work, this association of rotational distributions with scattering dynamics and features of the potential energy surface has been useful in interpreting product state distributions.

Related work on the reactions of atomic chlorine (^2P) with hydrocarbons has been carried out by several groups. Park *et al.*[16] measured cold rotational state distributions from the reaction of Cl with cyclohexane, and Yen *et al.*[17] measured similar rotational state distributions from the reaction of Cl with propane. Varley and Dagdigian[12] studied the reaction of atomic chlorine with hydrocarbons ranging from methane to isobutane and found all these reactions to produce cold rotational distributions. They also found the differential cross section for the reaction of Cl with isobutane to be mostly back scattered. These studies seem to indicate that atomic chlorine and atomic oxygen abstract hydrogen similarly from hydrocarbons, resulting in rotationally cold, presumably backscattered product. Similar conclusions have been reached for reaction of atomic fluorine with hydrocarbons.[18]

In our earlier investigations of the $HCl(v=1,J)$ products from the reaction of $Cl+CH_4(\upsilon_3=1)$, we found that the vibrationally excited product is both rotationally cold and predominantly forward scattered.[11] This counterexample to the association of cold rotational distributions with back scattering certainly should caution those who wish to infer angular-scattering information from internal-state distributions, but this result is quite likely related to the specifics of this reaction, especially the vibrational excitation of the reagent. To understand the reactivity more completely, we have applied higher resolution methods (see preceding paper) to the determination of state-to-state scattering in this system and have investigated the vibrationally unexcited product $HCl(v=0,J)$ and isotopically related reactions. Additionally, we have measured reactive alignment effects, such as the dependence of the reaction on the alignment of the rotational angular momentum, and of the C–H stretch vibration with respect to the direction of approach of the chlorine atom.

The investigation of the steric requirements for reactivity has had a long history.[2] If the molecule possesses a dipole moment, then electric fields can be used to effect orientation and alignment.[19–26] Studies by the research groups of Brooks, Bernstein, Loesch, and others have yielded special insight into the steric requirements of reaction. Polarized pumping techniques can also be used to cause reagent alignment. This method has been applied to several atom–diatom reactions including Li+HF and Sr+HF.[23–25,27] The polarized pumping technique has the additional advantage that molecules that have small or no dipole moments can be aligned. In the present study, we use plane-polarized infrared excitation of $CH_4(\upsilon_3=1)$ and $CHD_3(\upsilon_1=1)$ to align the C–H stretch in the laboratory. Because these molecules have trivially small dipole moments, the reorientation of the aligned reagents by the approach of the Cl atom at long distances is expected to be negligible. Consequently, the preparation of the vibrationally excited reagent should control the geometry of the transition state of the reaction. The combined information of the angular distribution, internal-state distribution, and alignment dependence leads to a detailed model for this reaction.

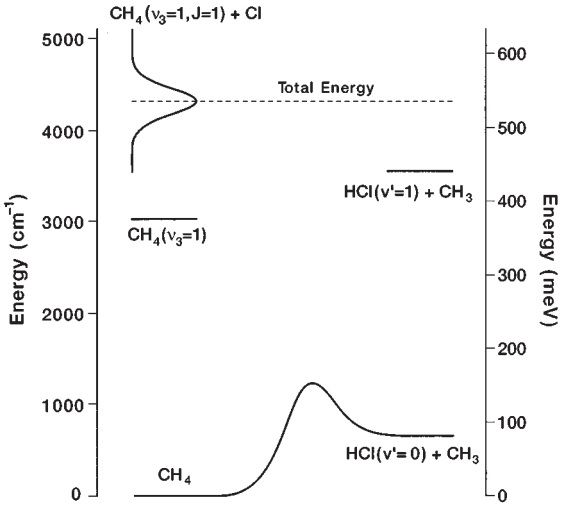

FIG. 1. The energetics of the $Cl+CH_4$ reaction. The collisional energy spread is represented by the Gaussian distribution that would result from a beam translational temperature of 15 K as calculated from the formulas of van der Zande *et al.* J. Phys. Chem. **96**, 8205 (1991).

II. BACKGROUND AND EXPERIMENTAL METHOD

The energetics for the reaction of atomic chlorine with vibrationally excited methane are relatively well established (Fig. 1). The $Cl+CH_4$ potential energy surface is slightly endothermic. In this paper, we have used the endothermicity $\Delta H=1.89$ kcal/mol (660 cm^{-1}, 0.082 eV),[28] which differs slightly (10%) from the value in the most recent physical chemistry reference data [$\Delta H=1.72$ kcal/mol (600 cm^{-1}, 0.075 eV)[29]]. This small change has practically no effect on the analysis presented here. The reaction has a small barrier of approximately 2.7 kcal/mol (940 cm^{-1}).[29] The height of the barrier was measured experimentally by many groups including Ravishankara and Wine,[9] who fit thermal rate data to an Arrhenius expression. High-level quantum mechanical calculations of the saddle point energy and geometry were carried out by Truong *et al.*,[10] and Dobbs and Dixon,[13] who found a barrier slightly higher than the preferred value but within the range of experimental rate data. Their calculations also indicated that the transition state was collinear along the Cl–H–C axis. For reactions of atomic chlorine with isotopically substituted methanes, the reaction endothermicities were calculated by using the harmonic approximation to correct for changes in zero-point energies. With this correction, the reaction of Cl with CHD_3 has an endothermicity of 800 cm^{-1}.

Chlorine atoms are produced with a monoenergetic speed distribution by the photolysis of molecular chlorine at 355 mm.[30,31] At this wavelength, the Cl_2 photolysis results in 98% ground-state $Cl(^2P_{3/2})$ atoms that react at a center-of-mass collision energy of 1290 cm^{-1} (0.159 eV). The slightly heavier mass of trideuteromethane target increases the center-of-mass collision energy of the chlorine atoms at the same photolysis wavelength to 1450 cm^{-1} (0.179 eV). Meth-

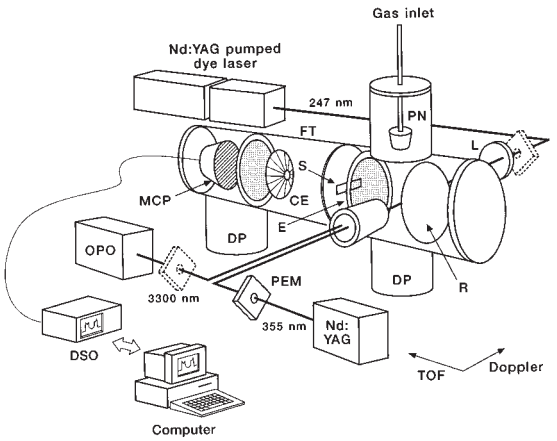

FIG. 2. Schematic diagram of the experimental apparatus. Abbreviations: CE: core extractor, DP: 6 in. baffled diffusion pump, DSO: digital sampling oscilloscope, E: extractor plate, FT: flight tube, MCP: microchannel plates, OPO: optical parametric oscillator, PC: personal computer, PEM: photoelastic modulator, PN: pulsed nozzle, R: repeller plate, S: slit.

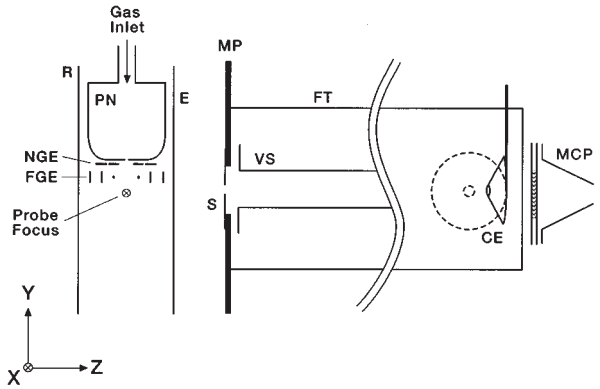

FIG. 3. Schematic diagram of the ion optics. The axes used for description of velocity distributions are shown in the bottom left corner, where *X* goes into the page. Abbreviations: CE: core extractor, E: extractor plate, FGE: field-guard electrodes, FT: flight tube, MCP: microchannel plates, MP: mounting plate, NGE: nozzle-guard electrodes, PN: pulsed nozzle, R: repeller plate, S: slit, VS: vertical steering plates. For the core extractor, the solid lines show position while core extracting, dotted lines show open position. The field-guard electrodes are resistively divided in potential so as to match the local field gradient caused by the extractor and repeller. The nozzle-guard electrodes are resistively divided to provide an even electrical potential drop across the face of the pulsed nozzle.

ane molecules are excited to the $\upsilon_3=1$ asymmetric C–H stretch by absorption of infrared light generated in a lithium niobate optical parametric oscillator (OPO). In the vibrationally induced reaction of Cl with CHD_3, the trideuteromethane was excited to the $\upsilon_1=1$ C–H stretch by infrared absorption centered at 2993 cm^{-1}.[32,33] This state is nearly isoenergetic with the asymmetric stretching mode of methane, ν_3 at 3019 cm^{-1}.[32–34] The energetic effects of the isotopic substitution are small, and overall, the reactions of atomic chlorine with vibrationally excited methane and trideuteromethane are quite comparable.

Figure 2 shows a schematic diagram of the experimental apparatus. Cl_2 (Matheson, research purity, 99.999%) was mixed with CH_4 (Matheson, ultra high purity, 99.97%) and He (Liquid Carbonic, 99.995%) in the ratio 1:3:4 of Cl_2:CH_4:He. Methane was further purified by delivery through a copper coil immersed in an ethanol slush bath, and helium was passed through a copper coil immersed in liquid nitrogen to remove condensable gases. The gas mixture was stored in a Teflon-lined stainless-steel mixing tank (Hoke) and expanded into high vacuum via a pulsed nozzle. The backing pressure of the pulsed nozzle was measured by a Baratron pressure gauge (MKS Instruments, 0–1000 Torr) and controlled by a metering valve. The pulsed nozzle (General Valve, series 9, 0.6 mm orifice diameter) was gold coated to minimize surface-catalyzed reaction of molecular chlorine with methane (and contaminant gases), and it was driven by a home-built controller. The backing pressure was stabilized at 380 Torr. The gas handling system was exhausted by a mechanical pump operating with perfluorinated pump oil (Fomblin, Y-VAC 25/6) trapped by activated alumina (Edwards), activated charcoal (Spectra Gases), and liquid nitrogen to eliminate contamination. These measures resulted in a significant decrease of hydrogen chloride contamination in the mixture but were not sufficient to completely eliminate the contamination. When the contamination caused background contributions to the signal, these contributions were minimized with subtraction procedures described later.

The high-vacuum system consists of a reaction chamber connected through a small slit to a differentially pumped detection chamber. The reaction chamber was pumped by a liquid-nitrogen-baffled 6 in. diffusion pump (Varian, VHS-6 with baffle) using perfluorinated diffusion pump oil (Fomblin Y-VAC 25/9). The reaction chamber had a base pressure of $\approx 5\times10^{-7}$ Torr, which typically rose to 1 to 2×10^{-5} Torr during experiments. The detection chamber was pumped by an identical diffusion pump and baffle using Santovac-5 pump oil and had a base pressure of $\approx 7\times10^{-8}$ Torr and an operating pressure of $<5\times10^{-7}$ Torr.

The mass spectrometer is a Wiley-McLaren two-stage acceleration design,[35] with some minor modifications. A schematic diagram of the time-of-flight mass spectrometer is shown in Fig. 3. All ion optics were made of type 304 stainless steel with 85% transmission stainless-steel electroformed mesh. A large repeller and extractor (115 mm diameter, 26.5 mm spacing) were used to ensure a uniform acceleration field across the extraction region. The electrically grounded pulsed nozzle was isolated from the acceleration fields by two layers of electrostatic shielding. This shielding allowed the pulsed nozzle to be placed 8 mm away from the laser-beam-crossing region with very little degradation of the linear acceleration field. The field homogeneity and Wiley-McLaren space-focusing condition were checked by measuring the time-of-flight shift of a HCl^+ peak as the ionizing laser beam was moved within the reaction region. Time-of-flight shifts were generally a few nanoseconds within 2 mm from the center of the region. One shield was mounted directly on the pulsed nozzle and consisted of four steel strips electrically connected by a series of resistors mounted in vacuum. The potential drop across this shield and shift of the center from electrical ground were controlled by

a power supply outside the vacuum. The second shield was part of the extractor–repeller combination and consisted of four metal strips and two wires that were electrically connected via a chain of resistors to provide the correct potentials for each electrode. This shield was wired directly to the repeller and extractor; therefore, its potentials were fixed by those of the extractor and repeller. The extractor–repeller combination was mounted adjustably to a plate that formed the wall of differential pumping between the reaction and detection chambers. This adjustment allowed exact alignment of the repeller and extractor with respect to the flight axis.

The reaction and detection chambers were separated by a defining slit, 7 mm high by 6 mm wide, that was mounted in the middle of the support plate and covered with mesh. Vertical and horizontal oversized steering plates (89 mm long, 65 mm wide, 20 mm separation) were mounted on rods on the detection side of the support plate. Vertical steering of the ions was necessary to compensate for the molecular-beam stream velocity. To steer the ions without fringe field effects, we used a pulsed steering plate to provide the steering field only when the ions of the mass of interest were in the center of the steering plates. The steering pulse was shaped to hold the steering plate at the same potential as the other steering plate when the ions of interest entered and exited, thereby eliminating fringe fields that would distort the directions of the ions. The time-of-flight tube (360 mm long, 85 mm diameter) was formed of perforated stainless-steel sheet to improve pumping speed and supported the core extractor on its end plate.

The core extractor was a truncated stainless-steel cone with a hole diameter of 6 mm; it was mounted on a swinging mount that allowed it to be placed either away from the flight axis, to measure total ion signal, or in core-extraction mode, centered along the flight axis. The position of this swinging mount was controlled by a vacuum manipulator that consisted of a bellows linear-motion feedthrough connected through a flexible Teflon tube coupler to a crank arm on the core extractor. The ions emerging from the end plate of the flight tube accelerated through 6 mm to a two-plate chevron microchannel plate detector (Galileo, 25 mm diameter plates). This ion signal was then coupled out of the chamber with a 50 ohm-matched coaxial cable. The ion optics were made perpendicular to the flight axis by retroreflecting a He–Ne laser off a mirror temporarily placed on each element of the spectrometer.

The vertical reagent beam from the pulsed nozzle was intersected at a distance of 8 mm from the orifice by the photolysis laser beam. The photolysis beam was generated by frequency tripling the output of a Nd^{3+}:YAG laser (Quantel YG-581, 20 Hz) to generate 355 nm light. For studies of the reaction of atomic chlorine with vibrationally excited methane, an infrared vibrational excitation laser beam was fired 15 ns after the photolysis pulse. This beam was generated by a home-built grating-tuned lithium niobate optical parametric oscillator (OPO) pumped at 1.064 mm by the fundamental of a long-cavity modified Nd^{3+}:YAG laser (Spectra Physics, DCR-1, 10 Hz). The OPO operated at 10 Hz, whereas the other lasers operated at 20 Hz so that every other shot could be subtracted to remove background contributions to the vibrationally excited reaction (as described later). The probe laser beam was generated by frequency doubling in β-barium–borate the output of a tunable dye laser (Spectra Physics PDL-3) operating on LD489 laser dye (Exciton) pumped by the frequency-tripled output of a Nd^{3+}:YAG laser (Spectra Physics DCR-2AG, 20 Hz). The probe laser was fired either 100 or 200 ns after the OPO beam to allow for product buildup. The probe was tuned to detect state specifically $HCl(v,J)$ product molecules on the $F\ ^1\Delta_2 - X\ ^1\Sigma^+$ (0,0) or (1,1) bands[36–40] or the $E\ ^1\Sigma^+ - X\ ^1\Sigma^+$ (0,1) band[36–41] by (2+1) REMPI. The state-selected photoions were then separated by mass and initial velocity in the mass spectrometer. The ion signal was preamplified (EG&G ORTEC, model 9301), and the time profile of the mass or masses of interest was digitized by a fast digital sampling scope (Hewlett-Packard, HP54542A) operating at 1 or 2 GSa/s. The scope accumulated a number of traces in its internal memory, then passed the signals to a personal computer (Los Altos Computers, 486 DX-33) over the GPIB peripheral interface.

Alternatively, for the checks of the core-extraction system presented in the previous paper, multiple photolysis wavelengths were used to produce ground-state Cl $^2P_{3/2}$ and spin–orbit-excited Cl $^2P_{1/2}$ atoms in a range of laboratory speeds and spatial anisotropies. Both 355 nm light obtained by tripling the output of the photolysis Nd^{3+}:YAG laser and 416 nm light generated by Stokes Raman shifting the 355 nm light in hydrogen gas (30 psi) were used to produce Cl atoms. The probe laser was fired approximately 20 ns after the photolysis pulse. The probe laser beam was tuned to ionize either ground-state Cl $^2P_{3/2}$ atoms at 240.53 nm or spin–orbit-excited Cl $^2P_{1/2}$ at 240.19 nm by (2+1) REMPI. The resultant photoions were then detected exactly as in the reactive studies.

The timing of the lasers, pulsed nozzle, and pulsed steering was controlled by home-built timing boxes and a digital delay generator (Stanford Research Systems, DG535) which set the precise timing of the laser time delays. The firing of the lasers was synchronized with the stress reference of a photoelastic modulator (Hinds International, PEM-80) so that polarization-dependent spectra could be taken on a shot-by-shot basis. A status signal that encoded the state of the photoelastic modulator and the presence or absence of an infrared pulse was sent to the digital scope. The computer used this status signal to generate shot-by-shot polarization-dependent data and infrared-induced difference data, or both.

III. RESULTS

The reactions of atomic chlorine with vibrationally excited methane and trideuteromethane were investigated using core extraction as described in the previous paper. Background HCl signals and nonresonant ions at neighboring masses were removed by subtracting data recorded with and without infrared laser excitation. This subtraction was made on an every-other-shot basis by operating the probe and photolysis lasers at 20 Hz while the OPO operated at 10 Hz. This every-other-shot subtraction procedure was checked for electronic error by verifying that no difference signal results

when the infrared beam is physically blocked. Background HCl($v=1,J$) from near-resonant vibrational energy transfer of OPO-excited methane molecules to HCl was reported in our previous study of this reaction.[11] As before, the background was subtracted by our fitting routine, which determined its contribution and then removed it from the data. Because we have eliminated a large fraction of the HCl contamination in our system, this background was not present in most data sets presented here and no energy-transfer subtraction was applied to these background-free data sets. Polarization data were taken using a photoelastic modulator to switch by 90° the linear polarization of one of the lasers on alternate pairs of ''ir on'' and ''ir off'' signals. This four-shot subtraction procedure was used to decrease our sensitivity to drifts in the signal intensity. Beam walk was avoided by using the photoelastic modulator, which is not physically moved in the experiment. Additionally, the power was not dependent on the state of the photoelastic modulator, so that we could compare absolutely the signal levels for the two measured polarizations. We tested for polarization-dependent power changes by recording the polarization difference for HCl($v=1$, $J=0$) excited on the $P(1)$ branch of HCl. Because the $J=0$ state cannot be polarized, no polarization difference should be observed on this excitation line, and our test showed no difference within error bars.

As described in the preceding paper, the extraction voltage determines the speed resolution and affects the signal intensity. Therefore, a range of voltage conditions, depending on the signal intensity, was used to record reactive time profiles. Three extraction voltage conditions, which we refer to as ''high resolution'' (69 V/cm), ''medium resolution'' (113 V/cm), and ''low resolution'' (169 V/cm) were used.

A. HCl product state distributions

Figure 4 shows the integral cross sections measured for the HCl(v,J) product of the reaction $Cl+CH_4(\upsilon_3=1) \rightarrow HCl(v,J)+CH_3$. HCl($v=1,J$) populations were measured by recording wavelength excitation spectra while detecting integral ion signal of the $m/z=1$ (H^+) peak from dissociative ionization of the HCl product on the $E-X$ (0,1) band.[36,41] This REMPI spectrum is converted to populations by correcting for fragmentation and linestrength changes with rotational state as described in Appendix A. The HCl($v=0,J$) populations were measured by recording spectra while detecting the $m/z=36$ ($H^{35}Cl^+$) peak intensity as the REMPI laser was scanned over the R branch of the $F-X$ (0,0)[36–40] band. Despite many attempts, we were unable to completely eliminate HCl contaminant from our system. This contamination precluded measurement for HCl($v=0$, $J=0$). Therefore, no data for this state is shown. On all other rotational states, our every-other-shot subtraction procedure removed this HCl background. The OPO every-other-shot subtraction procedure measures the difference caused by vibrational excitation. For HCl(v,J) states with no reactive background, this subtraction results in signal purely caused by the vibrationally excited reaction. We have observed the reaction of atomic chlorine with ground state methane, which populates HCl($v=0$, $J\leqslant 3$). Therefore, the populations shown in Fig. 4 for HCl($v=0$, $J\leqslant 3$) are technically the difference between the excited and ground state reactions. We have not corrected for the difference because it is well within the 2-σ error bars shown on the plot. Comparison of the ground-state and vibrationally excited reactions is the subject of a forthcoming paper.[42] The rotational population distributions were scaled with respect to each other by recording HCl($v=1$, $J=1$) intensity on the $R(1)$ branch of the $F-X$ (1,1) band in the same scan with HCl($v=0,J$) rotational distributions. The vibrational correction factor for relative detection sensitivity on the $F-X$ diagonal bands was measured as described in Appendix A. This vibrational correction factor was used to scale the $v=1$ and $v=0$ populations shown in Fig. 4. The rotational-state-integrated vibrational branching ratio of HCl $v=1$:$v=0$ is approximately 3:7.

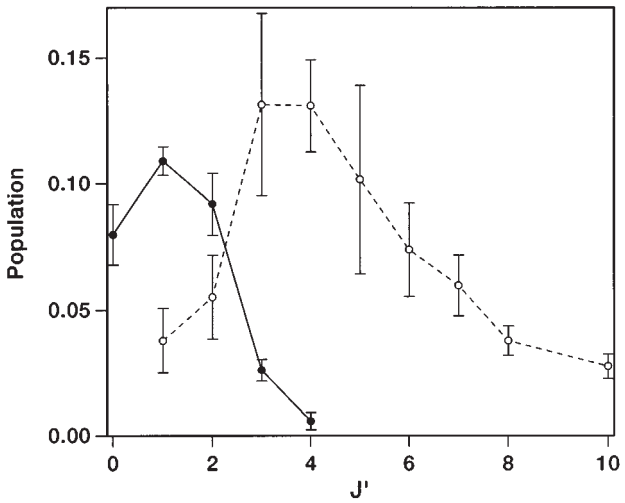

FIG. 4. Integral product state population distributions for the reaction of atomic chlorine with vibrationally excited methane. The HCl($v=0,J$) populations are represented by dotted lines and open symbols and the HCl($v=1,J$) populations by solid lines and filled symbols. The $v=0$ and $v=1$ populations are determined from REMPI spectra as described in the text. The error bars are $\pm 2\sigma$ statistical confidence intervals. Both the HCl($v=0,J$) and HCl($v=1,J$) population distributions are relatively scaled with respect to each other by using a vibrational correction factor as described in the text.

Figure 5 shows the analogous plot for the HCl product of the reaction of Cl with $CHD_3(\upsilon_1=1)$. DCl($v=0$, low J) from the reaction of Cl with ground state CHD_3 was observed. The DCl product showed no OPO-induced difference signal on any line probed, including both DCl($v=0$) and DCl($v=1$), indicating that the $Cl+CHD_3(\upsilon_1=1)$ reaction is bond specific. HCl populations were recorded by detection of $m/z=36$ integral ion signal on the $F-X$ diagonal bands. The distributions were more poorly determined than those of the methane reaction owing to the decrease in signal for this reaction. Experiments demonstrated an approximately eightfold decrease in HCl($v=1$, $J=1$) signal magnitude compared with that of the $Cl+CH_4(\upsilon_3=1)$ reaction. Because the infrared absorption cross section of $CHD_3(\upsilon_1=1)$ is approximately one fourth that of $CH_4(\upsilon_3=1)$,[43] and the population of HCl($v=1$, $J=1$) for $Cl+CHD_3(\upsilon_1=1)$ is roughly half of the $Cl+CH_4(\upsilon_3=1)$, this result indicates approximately the same reactivity for $CHD_3(\upsilon_1=1)$ and $CH_4(\upsilon_3=1)$. Because of possible statistical and systematic errors associated with com-

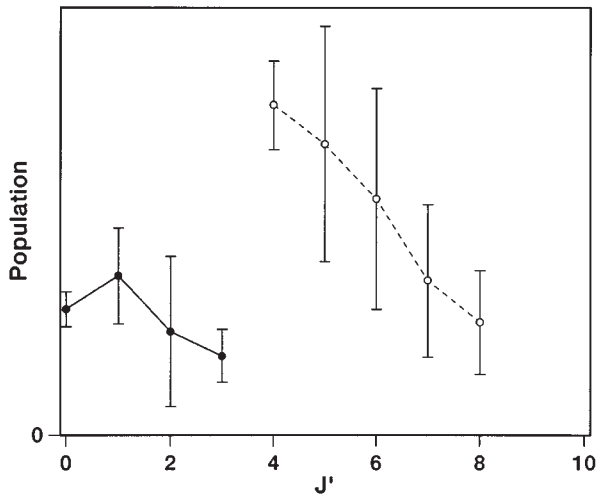

FIG. 5. Integral product state population distributions for the reaction of Cl with vibrationally excited trideuteromethane. The HCl($v=0,J$) populations are represented by dotted lines and open symbols and the HCl($v=1,J$) populations by solid lines and filled symbols. The HCl($v=0,J$) and HCl($v=1,J$) populations are determined from REMPI spectra as described in the text. The error bars are again $\pm 2\sigma$ standard deviations.

paring two different reactions, we hesitate to draw conclusions from this ratio. Rotational state distributions from both reactions are similar, with the HCl($v=1,J$) from $Cl+CHD_3(v_1=1)$ possibly slightly more excited. Assuming our fragments of the rotational state distributions are comparable, the vibrational branching ratio is significantly lowered for the $Cl+CHD_3(v_1=1)$ reaction when compared to $Cl+CH_4(v_3=1)$.

B. HCl product state-to-state scattering distributions

Time profiles for HCl products from the reaction of atomic chlorine with vibrationally excited methane were recorded and fit as described in the preceding paper. Rotational alignment of the HCl product was removed from the data by generating a linear combination of polarized signals that is nearly polarization free. We recorded $I_{\parallel}$ and $I_{\perp}$, where $I_{\parallel}$ is the signal when the probe laser polarization is parallel to the flight axis (taken to be the Z axis) and $I_{\perp}$ is that with the polarization crossed. We then analyzed the sum $I_{\parallel}+2I_{\perp}$, which eliminates the lowest order rotational alignment effect from the time profile when no higher order moments or coherences from other alignment effects are present. In our experiment, there may be coherences that result from the broken cylindrical symmetry that arises from the photodissociation laser and infrared laser polarizations. An analysis that includes a treatment of broken cylindrical symmetry and a measurement of the product rotational anisotropy is the subject of a forthcoming paper.[44] Error bars for the extracted speed distributions were determined by taking 95% statistical confidence intervals for the data pertaining to each spectral line. We recorded at least six reactive time profiles for each detected spectral line and performed measurements on multiple days in an effort to remove systematic errors in our purely statistical error intervals. All experimental data shown in this paper represent the coadded summation of all measurements on that spectral line because we found that coaddition of data significantly reduced the noise on the signal.

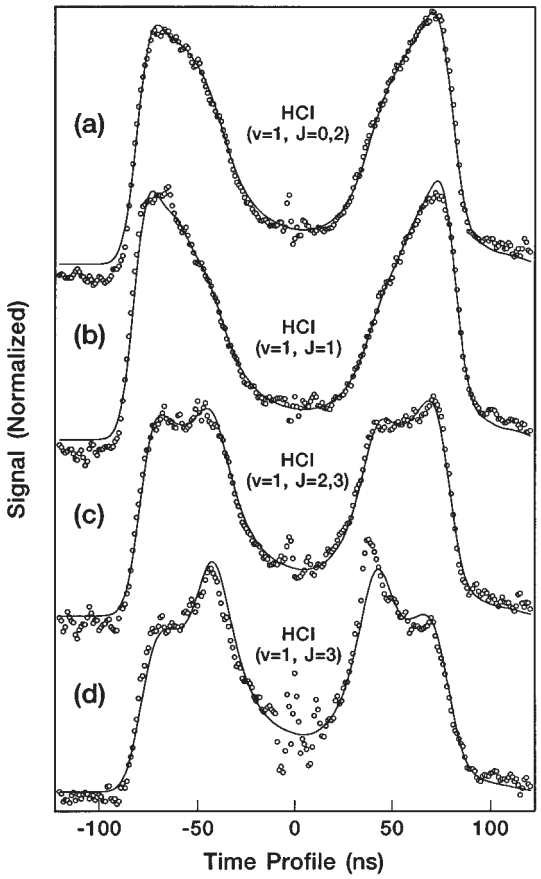

FIG. 6. Coadded core-extracted time profiles for detection of HCl($v=1,J$) on four lines of the $F-X$ (1,1) band from the reaction of Cl with $CH_4(v_3=1)$. (a) Detection of 67% $J=0$ and 33% $J=2$ on the $S(0)/R(2)$ blend line. (b) Detection of $J=1$ on the $R(1)$ line. (c) Detection of 78% $J=2$ and 22% $J=3$ on the Q-branch bandhead. (d) Detection of $J=3$ on the $R(3)$ line. Note that the $R(3)$ line of the $F-X$ (1,1) band is overlapped by the $D-X$ (0,0) $R(3)$ line, and subtraction of this background results in the scatter near 0 ns time shift. In all plots, the symbols show the experimental data, and the fits are shown as lines.

1. HCl($v=1,J$) differential cross sections

Figure 6 shows the coadded time profiles for HCl($v=1$) from the reaction of Cl with $CH_4(v_3=1)$ recorded on four lines of the $F-X$ (1,1) band: $S(0)/R(2)$ blend, $R(1)$, Q-branch bandhead [$Q(2)$ and above], and $R(3)$. The $CH_4(v_3=1)$ reagent was prepared by excitation on the Q branch to minimize reagent alignment effects that are described later. The data were taken at ''high resolution.'' Because of systematic overlap of S-branch lines with even-J R-branch lines, the signals for HCl($v=1$, $J=0,2$) could be recorded only on blended lines. The $S(0)/R(2)$ blended line primarily measures scattering for HCl($v=1$, $J=0$) molecules. Knowledge of the line strengths and measurement of populations described previously allows us to determine that 67% of this line is from $J=0$. Similarly, the Q-branch bandhead is 78% $J=2$ and 22% $J=3$. Corrections based on these assignments were applied to the speed distributions to extract

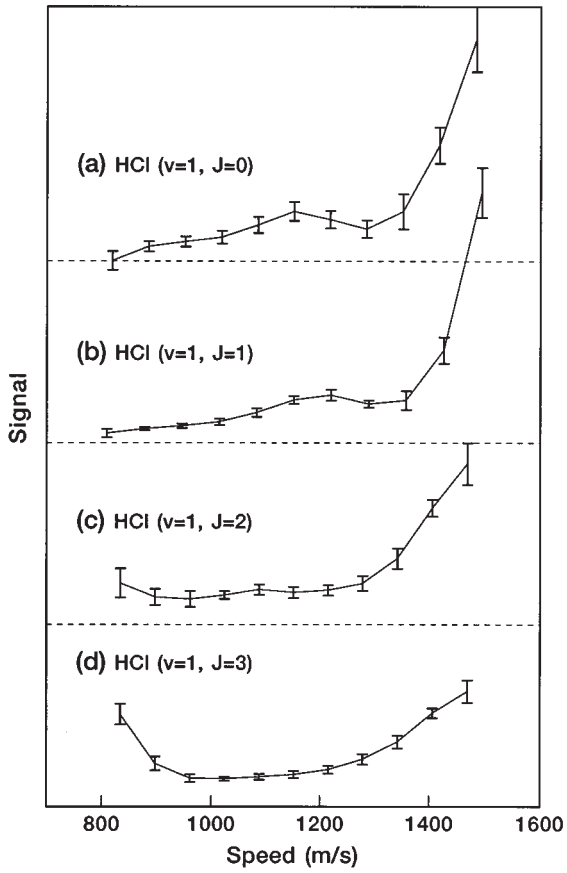

FIG. 7. Speed distributions for HCl($v=1,J$) from the reaction of Cl with $CH_4(v_3=1)$. (a) $J=0$ extracted from $S(0)/R(2)$ blend as described in text. (b) $J=1$ from $R(1)$ line. (c) $J=2$ extracted from Q-branch bandhead. (d) $J=3$ from $R(3)$ line. Error bars represent 95% confidence intervals as described in the text.

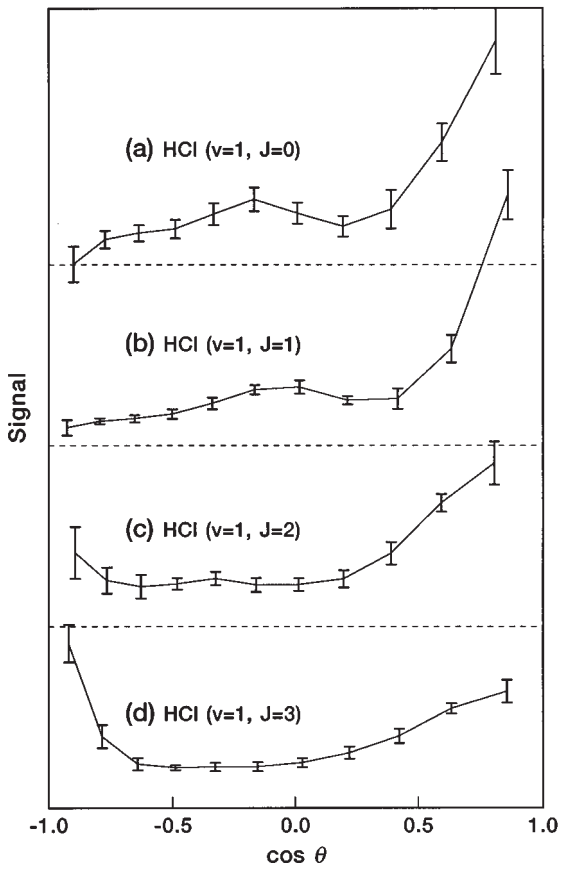

FIG. 8. State-to-state differential cross sections for the reaction $Cl+CH_4(v_3=1)\rightarrow HCl(v=1,J)+CH_3$. The data are converted from the speed distributions of Fig. 7 using the assumption of no kinetic energy release into the methyl radical. The curves are for (a) HCl($v=1$, $J=0$), (b) HCl($v=1$, $J=1$), (c) HCl($v=1$, $J=2$), and (d) HCl($v=1$, $J=3$).

the pure speed distributions for $J=0$ and $J=2$. These speed distributions along with those from $R(1)$ and $R(3)$ time profiles are shown in Fig. 7.

A trend is clearly visible in the reactive time profiles; the angular distributions shift toward back scattering with increasing J of the HCl($v=1$) products. The same trend is also clearly seen in the speed distributions. Close examination of Fig. 7 reveals a ''bump'' that seems to occur near 1200 m/s for HCl($v=1$) in the low J but disappears as J increases. Only the lowest frequency umbrella bending (the ν_2 mode) of the methyl radical is energetically accessible for the HCl($v=1,J$) product. Because excitation of this bending mode would remove nearly all the available energy from translation, the fastest and slowest products, corresponding to forward- and backscattered HCl($v=1,J$), cannot be formed in coincidence with vibrationally excited methyl radicals. For the lower rotational states, $J<3$, the region of the speed distribution near the center-of-mass speed (1150 m/s) could have contributions from HCl scattering in coincidence with methyl vibrational excitation. As an example, HCl($v=1$, $J=1$) formed in coincidence with one quantum of methyl umbrella vibration can appear between ± 180 m/s shifted from the center-of-mass speed. Therefore, the large peak near 1500 m/s could not possibly be formed in coincidence with methyl ν_2 excitation, but the bump near 1200 m/s could be associated with methyl excitation. For $J>2$, the methyl vibrational excitation channel closes because of the total energy constraint.

These speed distributions can be converted to differential cross sections by the methods described in the preceding paper. Performing this inversion requires an assumption about the energy deposition into the unobserved product. For HCl($v=1,J$), the kinematics of this reaction imply that the experimentally measurable spatial anisotropy is of little aid in constraining the methyl vibrational excitation. For this reason and also because most of the HCl($v=1,J$) product intensity occurs at speeds farther from the center-of-mass speed than is possible in coincidence with methyl vibrational excitation, we assume the methyl radical consumes no energy and all the excess is present in translation. Under this assumption, we arrive at the differential cross sections shown in Fig. 8. Again, the shift in product scattering behavior with rotation is observed. Any HCl($v=1,J$) product that was actually formed with methyl vibrational excitation would appear near the side-scattered region of this plot. The small bump near $\cos\theta=0$ may be some evidence for the existence of a small amount of vibrationally excited methyl in the HCl($v=1$, $J<3$) products. If these bumps are in fact formed in coincidence with vibrationally excited methyl radicals, then the bump intensity would be decreased and that inten-

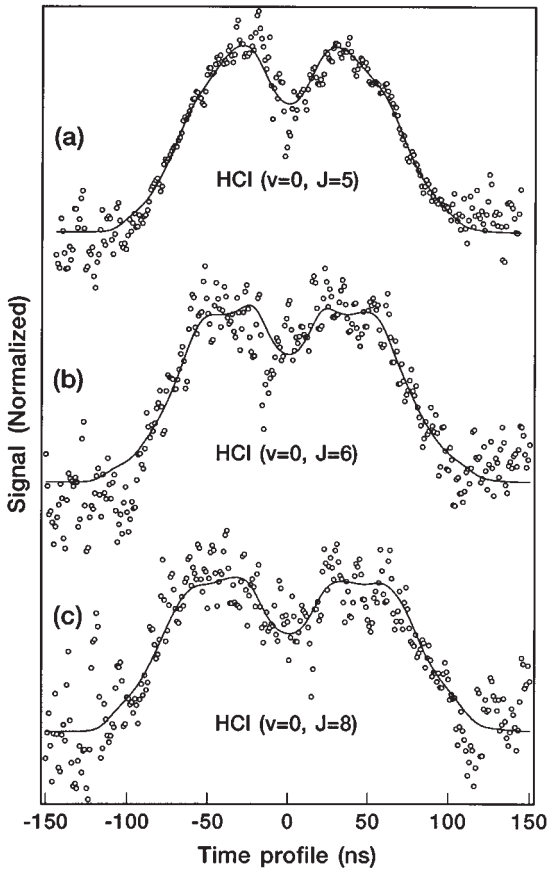

FIG. 9. Coadded core-extracted time profiles for detection of HCl($v=0,J$) on selected lines of the $F-X$ (0,0) band from the reaction of Cl with $CH_4(\upsilon_3=1)$. (a) Detection of $J=5$ on $R(5)$. Note that the central region has increased noise from subtraction of large background HCl on this line. (b) Detection of $J=6$ on $R(6)$. (c) Detection of $J=8$ on $R(8)$. In all plots, the symbols show the experimental data, and the fits are shown as lines.

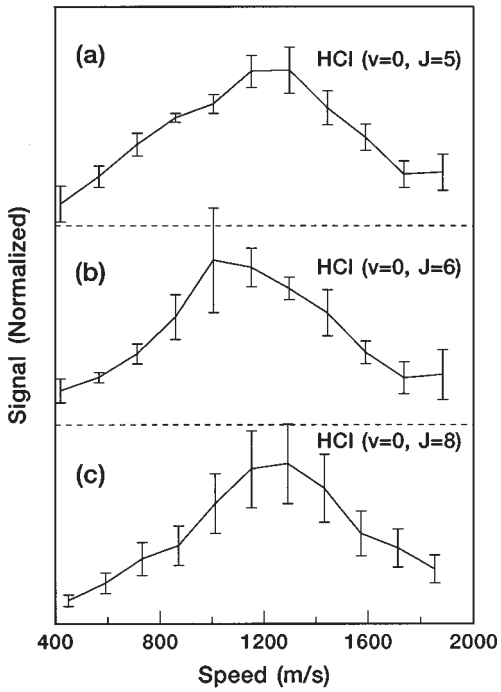

FIG. 10. Speed distributions resulting from the fits to the data shown in Fig. 9. Error bars are again 95% confidence levels based on mutual deviations between replicate data sets. For HCl($v=0$, $J=8$) we do not have enough replicate measurements to determine 95% confidence levels. Therefore, we have estimated ±25% error as an approximate error. The curves are for (a) HCl($v=0$, $J=5$), (b) HCl($v=0$, $J=6$), and (c) HCl($v=0$, $J=8$).

sity would be spread across the differential cross section. Clearly, however, this feature is small if it even exists and thus does not change the conclusions that (1) the HCl($v=1,J$) product is predominantly forward scattered and that backscattering rises to rival the forward peak as the rotational quantum number increases and (2) little if any methyl vibrational excitation occurs.

2. HCl($v=0,J$) differential cross sections

Figure 9 shows core-extracted time profiles for selected rotational states of HCl($v=0,J$) from the reaction of vibrationally excited methane detected via R-branch lines of the $F-X$ (0,0) band. Perturbations of the line strengths described by Xie *et al.*[37] reduce the reactive signal for most of these lines, which leads to decreased signal-to-noise ratios for these states. Additionally, jet-cooled HCl contaminant background is significant for the lower J signals ($J<6$); this background contaminant is removed by our every-other-shot subtraction procedure. Because this jet-cooled HCl contaminant has nearly zero velocity, subtraction of the background leads to increased noise near the zero time shift. Unlike the HCl($v=1,J$) product, the signals change little with J and, if anything, they shift toward increased product at high laboratory speed as J increases, implying that rotationally excited products may be more forward scattered than the lower rotor states. This trend is expected for an impulsive release model such as that proposed by Andresen and Luntz[14,15] in the reaction of O(^3P) with hydrocarbons.

The speed distributions that result from time-profile analysis are shown in Fig. 10. The weak trend of increased forward scattering for higher J products is within the error bounds of the measurement. Note that the volume element correction [Eq. (6) of the preceding paper] that was required to convert these signals from speed distributions to scattering distributions is quite significant because a larger range of laboratory-frame product speeds is available to these HCl($v=0,J$) products than is available to the HCl($v=1,J$) products shown previously. To convert these speed distributions to differential cross sections, we need to consider the possibility of excitation of the methyl radical.

Measurement of the spatial anisotropy of the product measures the off-axis nature of the scattering with respect to the collision frame as described in the preceding paper. We have measured the spatial anisotropy of the product for the HCl($v=0,J$) products of this reaction by recording core-extracted time profiles with the photodissociation laser nearly parallel (8°) and perpendicular (98°) to the flight axis.[45] Observation of the off-axis projection allows for determination of the internal energy deposited into the unobserved methyl product. The shaded area of Fig. 11 shows the region of possible internal energy releases versus the speed of the observed HCl product. The top of the parabola repre-

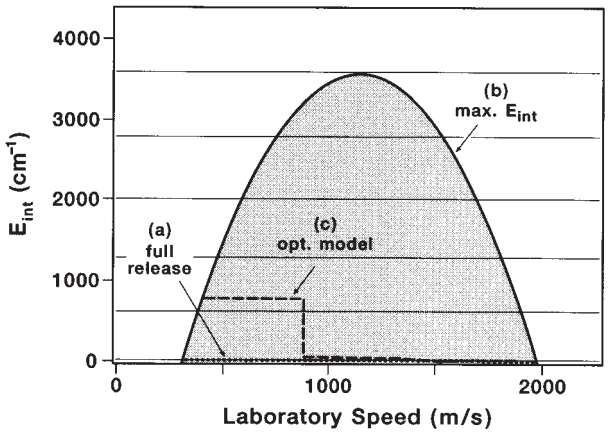

FIG. 11. Region of possible internal energy releases to the unobserved methyl product as a function of the observed speed of the HCl product from the reaction $Cl+CH_4(v_3=1)\rightarrow HCl(v=0,\ J=3)+CH_3$. The thin horizontal lines represent the methyl ν_2 umbrella mode vibrational energy levels. Curve (a), the narrow dotted line (labeled full release), shows no excitation of methyl. Curve (b), the solid line (labeled max E_{int}), shows the maximal possible excitation of methyl subject to the total energy constraint. Curve (c), the long dashed line (labeled opt. model), shows an optimized form as described in the text.

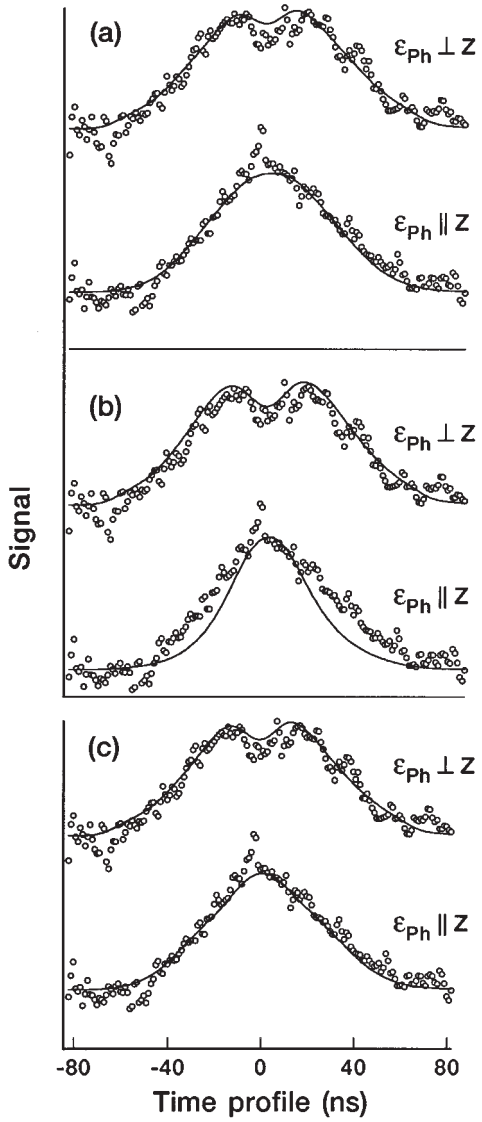

FIG. 12. Photodissociation polarization dependence of the reactive core-extracted time profiles for the reaction $Cl+CH_4(v_3=1)\rightarrow HCl(v=0,\ J=3)+CH_3$ recorded under medium resolution conditions. Parallel signals are recorded with photodissociation polarization (ϵ_{Ph}) 8° from the flight axis (**Z**), and perpendicular signals are recorded at 98°. Experimental signals are shown in points, and the parallel and perpendicular signals are vertically offset for clarity. Panel (a) represents no methyl excitation, (b) represents maximal methyl excitation subject to the total energy constraint, and (c) represents an optimized form as described in the text.

sents the case in which all the available energy is deposited into internal energy, leaving the HCl product motionless in the center-of-mass frame, which corresponds to a laboratory speed equal to the center-of-mass speed. When the HCl product has speed in addition to the center-of-mass speed, this condition requires kinetic energy, which decreases the amount of energy available for internal energy of the unobserved product. This conservation-of-energy limit is what forms the inverted parabolic border of the graph, curve (b). The other possible limit is that no internal energy appears in the unobserved product, which forms the bottom border of the graph. For any point within this parabolic region, we can predict the spatial anisotropy associated with that internal energy release and HCl speed. (See the preceding paper for discussion of this method.) For the fit, we use various forms of the internal energy release [i.e., curves (a), (b), or (c) in Fig. 11] to predict the spatial anisotropy versus speed, which is then used to generate parallel and perpendicular basis sets. These basis sets are used in the fitting of the differential cross section. Error in the selection of the form of the internal energy release causes inability to fit parallel and perpendicular data simultaneously.

Figure 12 shows the reactive signal for $Cl+CH_4(v_3=1)\rightarrow HCl(v=0,\ J=3)+CH_3$ in roughly parallel (8°) and perpendicular (98°) geometries recorded at "medium resolution" along with fits to various models of the dependence of the spatial anisotropy with speed. As before, the differential cross section is free to vary in these fits of photodissociation-polarization data. The curves in panel (a) show the fits to parallel and perpendicular signals assuming the methyl product to be completely unexcited. As with each set of curves in this figure, this model corresponds to the same named curve of Fig. 11. Note that this limiting assumption fits the data well, which demonstrates that the methyl product is not highly excited. Only the slow laboratory speed product, which corresponds to back scattering in the center-of-mass frame and appears near 0 ns, shows significant deviation. The curves in panel (b) represent the fit with maximal internal energy release into the methyl product. Note that the data are inconsistent with this assumption by the clear deviation at the higher speeds (the wings of the plot of $\epsilon_{Ph}\|\mathbf{Z}$) and that the backscattered region is slightly better represented by this model than by model (a). We believe that this improvement for slow products points to increased internal excitation of the methyl radical product for the backscattered HCl trajectories.

To make a model with a better overall fit, we created curve (c) of Fig. 11 which has two levels of internal excita-

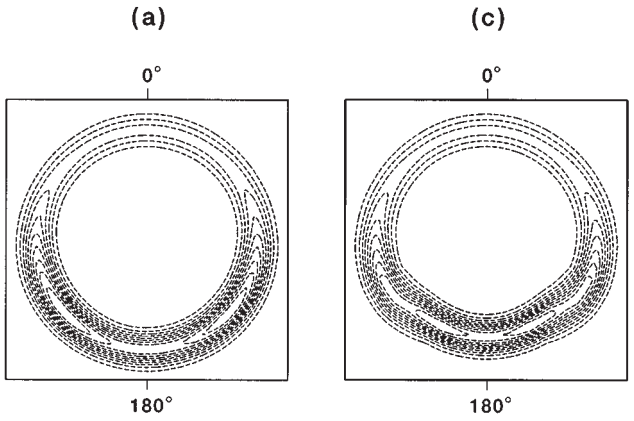

FIG. 13. Flux contour maps of scattering distributions for the polarization data presented in models (a) and (c) of Fig. 10 for the reaction of atomic chlorine with vibrationally excited methane leading to HCl(v=0, J=3). (a) The scattering with no methyl excitation. (c) The optimized model including variation of the methyl excitation across the differential cross section as described in the text.

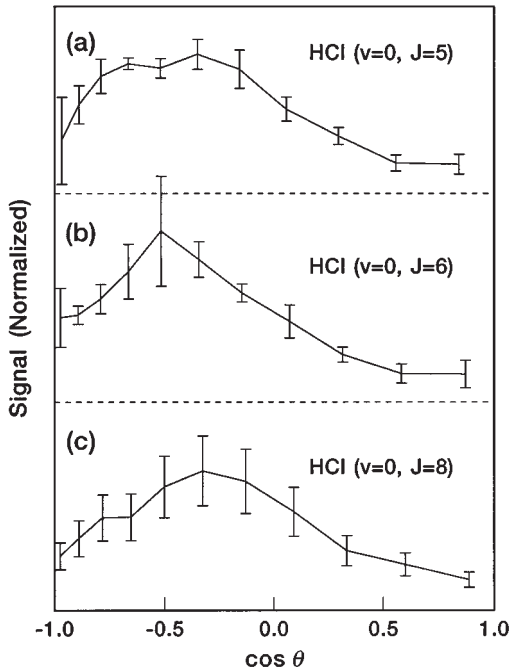

FIG. 14. State-to-state differential cross sections for the reaction $Cl+CH_4(\upsilon_3=1)\rightarrow HCl(\upsilon=0,J)+CH_3$. The data are converted from the speed distributions of Fig. 10 using the optimized kinetic energy release shown in Fig. 11. This internal energy deposition was determined by fitting of the photodissociation polarization dependence as described in the text. Whether the inversion is performed with this form for the energy release or performed under the assumption of absolutely no internal energy release to the product, only subtle changes to the state-to-state differential cross sections shown here occur. The curves are for (a) HCl(v=0, J=5), (b) HCl(v=0, J=6), and (c) HCl(v=0, J=8).

tion, one for the backscattered product and one for the side- and forward-scattered products. The fit with this model [panel (c) of Fig. 12] shows that this model partially repairs the fit in the central region of the scattering, lending credence to the idea of variation of methyl excitation across the differential cross section. There is still some discrepancy in the central region in this fit, that is likely caused by the simplicity of our model and possibly by subtraction error because this line has a significant background signal from HCl contamination in our mix. We used such a simple model because significant uncertainty exists in the determination of the internal energy deposition. Fits where we shift the internal energy deposition by hundreds of wave numbers are equally good. Additionally, the anisotropy is inherently an averaged quantity, and it determines a weighted average of the energetic deposition so that the actual form of this distribution cannot be uniquely determined. With these limitations in mind, we note that significant methyl excitation is clearly precluded by our measurements.

The speed distributions from the fits of Fig. 12 are used to create flux contour maps for HCl(v=0, J=3). Figure 13 shows these maps for models (a) and (c) of Fig. 12. Model (b) was rejected on the basis of poor fitting of the anisotropy data and is not included in Fig. 13. For both kinetic energy release models, the HCl(v=0, J=3) product is seen to be preferentially back and side scattered. The effect of allowing internal excitation of the methyl product in the backscattered region is to remove translational energy from the HCl product, which acts to flatten the circle in the backscattered region for fit (c). The differential cross section in both of these models is the same within error bars.

Spatial anisotropy polarization data recorded on other spectral lines of the HCl(v=0) product of this reaction are also effectively fit by the optimized model (c). For this reason, we have used this simple kinetic energy release model to convert the speed distributions of Fig. 10 to differential cross sections. Figure 14 shows the result of this conversion for selected rotational states of HCl($v=0,J$) from the reaction of vibrationally excited methane. These results show that the vibrational state of the HCl product drastically changes the differential cross section. The HCl($v=0,J$) product clearly lacks the sharp forward peak of the vibrationally excited HCl($v=1,J$) product, and the maximal intensity shifts toward back and side scattering. Possible origins for this observation are considered in the discussion.

C. Reagent alignment effects

Selection of the rotational branch on which the reagents are vibrationally excited controls the rotational state, the alignment of the distribution of rotational axes in space, and the C–H stretch alignment. The molecular properties are aligned with respect to the polarization vector of the excitation; therefore, rotation of the infrared polarization controls the alignment of the reagents in the collision frame. Because the core-extraction technique detects only products along the flight axis, this alignment of the molecule in the laboratory frame can be used to measure the dependence of the reaction on the alignment of molecular properties as a function of the scattering angle. As described later, core extraction is critical for sensitive measurement of reagent alignment effects; Doppler or noncore-extracted measurements would show greatly diminished effects because of greater averaging over reagent directions.

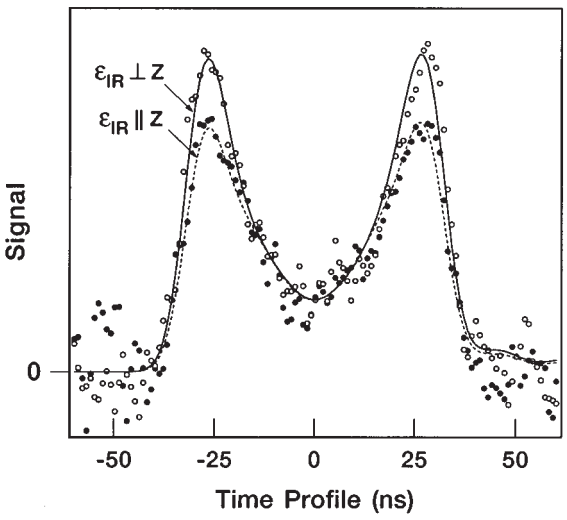

FIG. 15. Cl+CHD_3(v_1=1, Q-branch excited) infrared polarization effect for HCl(v=1, J=1). The solid line and open dots represent the experimental time profile for the polarization geometry in which the infrared laser is perpendicular to the flight axis ($\epsilon_{ir} \perp \mathbf{Z}$). The dashed line and filled in dots show the time profile for the parallel polarization geometry ($\epsilon_{ir} \| \mathbf{Z}$). The only difference between the two time profiles is the direction of the polarization of the infrared laser, yet the signal is changed both in intensity and shape. The data are taken using a photoelastic modulator to rotate the polarization. Therefore, the infrared intensity is equal in both spectra and the change in signal intensity is caused by a change in reaction probability that results from the polarization of the vibrationally excited methane reagent.

Trideuteromethane was selected for this study because infrared excitation of this molecule with linearly polarized light preferentially selects the direction of the single C–H bond of this molecule. Thus, observation of the HCl product can be related uniquely to the C–H stretch alignment. As discussed later, the vibrational amplitude of methane is also aligned by the infrared excitation, and the dependence of the reactivity with atomic chlorine on the reagent alignment can be studied. The interpretation of these methane vibrational alignment effects is more difficult because HCl product could have possibly come from any of the four hydrogen atoms in the methane molecule and not simply C–H bonds parallel to the vibrational alignment. For this reason, we first discuss the vibrationally induced trideuteromethane reaction and then the methane reaction.

1. Cl+CHD_3(v_1=1)

Figure 15 shows two time profiles for the HCl(v=1, J=1) product of the reaction of Cl with CHD_3(v_1=1, Q-branch excitation) in polarization geometries in which the electric vector of the infrared excitation (ϵ_{ir}) is chosen to be parallel or perpendicular to the flight axis (the Z axis). Under our experimental conditions, Cl+CHD_3(v_1=1) yields approximately eight times less HCl(v=1, J=1) product than Cl+CH_4(v_3=1). Consequently, we increased the extraction field for the trideuteromethane reaction to obtain sufficient signal, but this increase reduced our experimental resolution. Even under this ''low resolution'' condition, Fig. 15 shows that the HCl(v=1, J=1) product flux changes as the ir polarization direction is rotated by 90°. Thus the anisotropy of the vibrationally excited trideuteromethane molecules induced by the linearly polarized infrared excitation must affect the probability of chemical reaction. Because alignment of both the rotational axis and the C–H stretch axis of the excited molecules is induced by the excitation process, we must first understand rotational and vibrational alignment caused by ir excitation before we can distinguish these effects.

a. Rotational and vibrational alignment of CHD_3(v_1=1) resulting from ir excitation. In Appendix B we present the well-known result[46] of the degree of rotational alignment versus excitation line. For a review article on alignment effects and spherical tensors, see Orr-Ewing and Zare.[47] Q-branch excitation preferentially aligns **J** parallel to the electric vector of the light beam for linearly polarized light, whereas R- and P-branch excitation favors **J** perpendicular to the polarization direction. A convenient means of expressing the degree of alignment is by the $A_0^{(2)}$ moment, defined as

$$A_0^{(2)} = \langle 3\ \cos^2\ \gamma_J - 1 \rangle, \tag{1}$$

where γ_J is the angle between **J** and ϵ_{ir} and $\langle\ \rangle$ represents an ensemble average. Note that this moment completely describes the rotational alignment from one-photon infrared excitation with linearly polarized light. After excitation, the probability of finding the **J** vector of the vibrationally excited ensemble pointing at angle γ_J with respect to ϵ_{ir} is

$$P_{\mathbf{J}}(\gamma_J) = \frac{1 + A_0^{(2)} P_2(\cos\ \gamma_J)}{4\pi}. \tag{2}$$

Figure 16 presents the rotational alignment for a given *excited state J* as a function of excitation branch. We see that R- and P-branch excitation yield negative values of $A_0^{(2)}$ whereas Q-branch excitation yields positive values. Moreover, the degree of alignment rapidly approaches a limiting value with increasing J. The inset panel in Fig. 16 pictures spatial locations of a number of rotational axes following excitation on R, P, or Q branches in the vector model.

Alignment of the C–H stretch axis is a consequence of the excitation probability being proportional to $|\mu \cdot \epsilon_{ir}|^2$. In trideuteromethane, we excite the parallel band ν_1, which has its transition moment parallel to the C–H bond. Therefore, we preferentially prepare states that have their rotationally averaged transition moments, and stretching C–H bonds, parallel to ϵ_{ir}. The alignment of the molecular axes following this one-photon excitation in the frame of the linear polarization of the excitation light can be shown to be of the simple form

$$P_{\mathbf{v}}(\gamma_\nu) = \frac{1 + \beta_{\text{axis}} P_2(\cos\ \gamma_\nu)}{4\pi}, \tag{3}$$

where β_{axis} is dependent on the rotational line used to excite the molecule and γ_ν is the angle of the C–H stretch axis from ϵ_{ir}. Appendix B describes the calculation of the C–H stretch alignment that would result from excitation of a symmetric top on a parallel band with unresolved K structure neglecting nuclear spin. Figure 17 shows the result of this calculation of the averaged C–H stretch alignment versus the prepared state rotational quantum number J_f. The interesting result of this calculation is that for all rotational states and all excita-

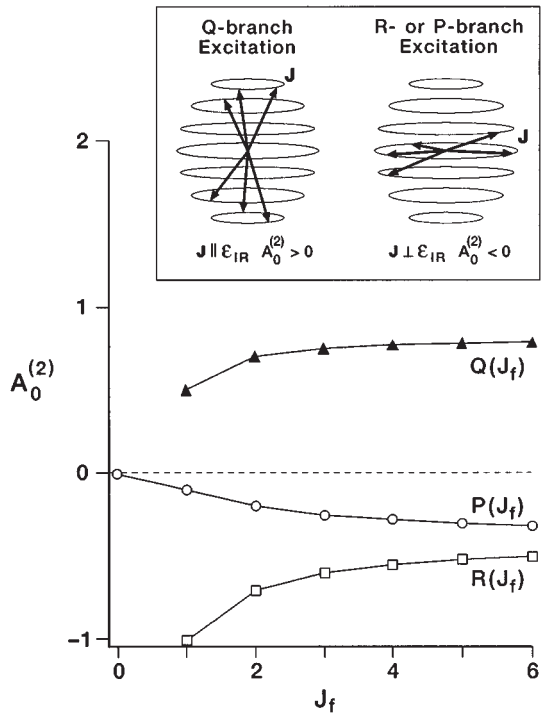

FIG. 16. Calculation of the rotational axis alignment $A_0^{(2)}$ of a molecule following unsaturated one-photon excitation using linearly polarized light. Alignments for *P*-, *Q*-, and *R*-branch excitation are labeled on the graph. The $A_0^{(2)}$ moment is plotted versus the rotational quantum number of the state prepared by the absorption process. The vertical axis ranges over the classical limits of this alignment parameter, -1 to 2. The inset panel shows schematic drawings of the rotational axis alignment induced by polarized excitation. In this panel, the electric vector of the preparation laser is vertical. The two columns represent excitation on either the *Q* branch or the *R* or *P* branches. The seven ovals represent the possible M_j states for this $J=3$ example. The vectors show the rotational vectors preferentially excited on each branch. The *Q* branch is seen to result in a positive $A_0^{(2)}$ moment with preferential excitation of **J** vectors parallel to the electric vector. *R*- and *P*-branch excitation show a negative $A_0^{(2)}$ moment with preferential excitation of **J** perpendicular to ϵ.

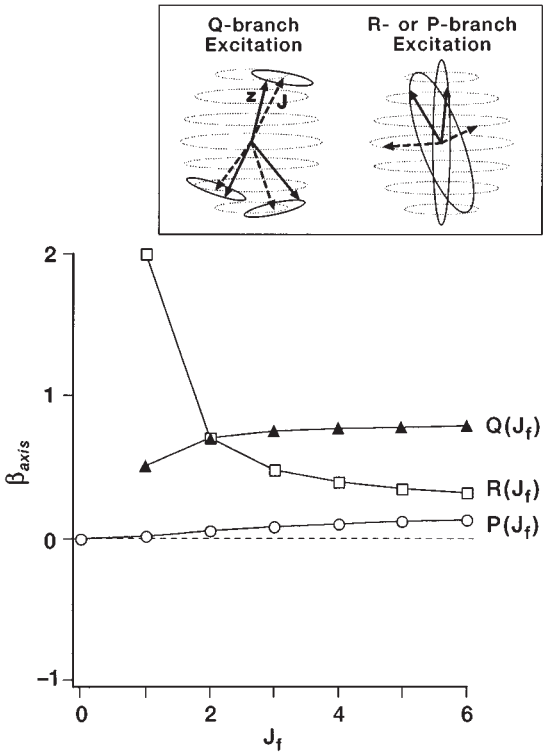

FIG. 17. Calculation of the bond alignment of a symmetric top following unsaturated one-photon excitation using linearly polarized light on a parallel branch where all *K* states are excited based on their linestrength; i.e., with no resolution of *K* upon excitation. This calculation is correct for a symmetric top with no nuclear spin statistics. Bond alignments for *P*-, *Q*-, and *R*-branch excitation are labeled on the figure. β_{axis} is plotted versus the rotational quantum number of the state prepared by the absorption process. The vertical axis ranges over the classical limits for this expectation value, i.e., -1 to 2. The *Q* branch can be seen to have a rapidly saturating axis alignment as *J* increases, whereas the *R* branch has perfect alignment at low rotor states that decays rapidly to its limit of 1/4 of the *Q*-branch limit. The inset panel shows schematic drawings of the vibrational axis alignment induced by this excitation. The electric vector of the preparation laser is vertical. The columns represent excitation on either the *Q* branch or the *R* or *P* branches. The seven ovals represent the possible M_j states for this $J=3$ example. The vectors show the **J** vectors following excitation on the respective branch in dashed lines with the molecule fixed top axis (**z**) shown precessing around **J**. The *Q* branch preferentially excites high values of *K* and thus large projections of **J** onto **z**. This interaction leads to tight precession of **J** around **z** with **J** precessing around ϵ, overall giving axes parallel to ϵ. The resultant β_{axis} is positive. The *R* and *P* branches excite low values of *M* and *K*, making two perpendicular interactions, which again leads to a positive β_{axis} as described in the text.

tion branches, the C–H stretch alignment distribution is preferentially parallel to the excitation polarization direction. This result is a consequence of the preferential excitation of molecules with rotationally averaged projections of the C–H stretch parallel to the excitation polarization. The exact nature of the rotational averaging that leads to these preferentially parallel states is different, however.

Q-branch excitation prepares states with rotational vectors close to parallel to the ϵ_{ir} and the C–H stretching axis tightly precessing around the **J** vector. These states correspond to C–H axes that point roughly parallel to the electric vector and the CD_3 group spinning like a top around the C–H stretching axis. This motion is shown in the *Q*-branch excitation vector drawing in the inset panel of Fig. 17. The rotation does not break the parallel nature of this interaction. The *R*- and *P*-branch axis alignment arises from a tumbling interaction that averages to a parallel alignment, but classically, the C–H bond swings through parallel and perpendicular states during every rotational period. A vectorial representation of this motion is shown in the *R*- or *P*-branch excitation cartoon in the inset panel of Fig. 17.

Hyperfine depolarization can be neglected, as we will explain. It could reduce the degree of alignment of trideuteromethane molecules following absorption of infrared plane-polarized light by coupling the nuclear-spin angular momentum to the rotational angular momentum.[48] Because the nuclear-spin angular momentum is initially unpolarized, this coupling dilutes the prepared alignment by mixing it with the randomly oriented nuclear spins. The order of magnitude of the time scale for this mixing is the Fourier transform of the splittings between the hyperfine levels. Although the hyperfine splittings for CHD_3 have not been measured, the largest hyperfine splitting constant of the CH_3D molecule arises from the deuteron, which is characterized by the quadrupolar coupling constant $eqQ=192$ kHz.[49] The Fourier transform

of the largest energetic splitting caused by the deuteron is approximately 5 μs; therefore, CHD_3 should show little if any hyperfine depolarization on the reactive time scale ($\leqslant$200 ns). For this reason, we believe that no significant hyperfine depolarization occurs for the trideuteromethane on the time scale of our experiment. Additionally, we have performed the experiment at half the pump–probe time delay and found the same result, again pointing to no significant depolarization.

b. Determination of origin of the CHD_3 alignment effect. These calculations show that the alignment of the C–H stretch peaks parallel to the laser polarization for all excitation branches, whereas the rotational axis alignment changes when switching between Q- and R-branch excitation. Therefore, we can crudely separate rotational and vibrational alignment effects by recording time profiles while exciting molecules on both of the Q and R branches and switching by 90° the linear polarization of the excitation laser. Effects that change in coincidence with polarization rotation but not branch switching are primarily C–H stretch alignment effects, and effects that change with excitation branch and with polarization rotation are primarily rotational alignment effects.

Examination of Figs. 16 and 17 shows that Q-branch excitation results in a positive C–H stretch alignment moment with a positive rotational alignment moment, whereas R-branch excitation results in a positive C–H stretch alignment moment and a negative rotational axis alignment moment. Figure 15 compares the reaction time profiles for the parallel and perpendicular ir polarization geometries with the $CHD_3(v_1=1)$ prepared by Q-branch excitation. By switching excitation from Q-branch to R-branch excitation, we change the sign of the rotational alignment moment while conserving the C–H stretch alignment direction. These calculations of the C–H stretch alignment produced by excitation of CHD_3 on various branches show that $R(0)$ excitation results in the strongest alignment, but we were not able to excite trideuteromethane on this spectral line because the $J=0$ initial state of this transition does not seem to be significantly populated in our expansion. Therefore, in Fig. 18 we measured parallel and perpendicular signals using the $R(1)$ spectral line for excitation of $CHD_3(v_1=1)$ with the opposite rotational alignment as was shown in Fig. 15 (Q-branch excitation). Although the signal-to-noise ratio is poor, the data again show stronger signal in the perpendicular collisional geometry. Taken together, Figs. 15 and 18 imply that the $CHD_3(v_1=1)$ alignment effect is primarily caused by C–H stretch alignment and not rotational alignment. Because the C–H stretch alignment peaks parallel to the infrared polarization, the increased signal in the perpendicular polarization geometry shows that perpendicular collisions of Cl atoms into the excited C–H bond enhances scattering into HCl(v=1, J=1).

c. Quantitative C–H stretch alignment analysis. Because the alignment effect seems primarily vibrational in origin, we developed a model in which C–H stretch alignment alone is responsible for the polarization effect. This model allows quantitative extraction of the probability of reaction as a function of approach angle from the vibrationally excited C–H bond. Let us define this reactivity by $R_v(\omega)$, where ω is the angle between the C–H stretch axis and the approaching chlorine atom. In our core-extraction experiment, the direction of the Cl atom is not fixed in space; instead, the HCl product direction is defined by the flight axis. However, flight-axis-aligned HCl products can come only from a subset of Cl atom directions. For example, forward-scattered HCl(v=1, J=1) results from parallel addition of the HCl product velocity in the center-of-mass frame to the velocity of the center of mass. Therefore, the laboratory-frame HCl velocity is parallel to the velocity of the reacting Cl atom, and detection of flight-axis-aligned HCl products selects reactions in which the Cl atom is parallel to the flight axis. In the more general case, the kinematics dictate that the angle between the Cl direction in the laboratory and the HCl(v=1, J=1) product direction varies between 0° and 20° depending on the scattering angle (the deflection angle is the angle α from Fig. 1 of the preceding paper). Therefore, all flight-axis-aligned HCl(v=1, J=1) products result from collisions with Cl atoms originally moving less than 20° off the flight axis. This selective detection of the product is one of the great advantages of core extraction; without core extraction, the alignment effect would be measured not for the highly selected Cl atom directions of core extraction but for the weakly selected Cl atom directions induced by the anisotropy of the photolysis of Cl_2. Because the Cl atoms from the photolysis fly in many directions, the alignment effect would be integrated over all these directions, diminishing its observed magnitude. Core extraction replaces this integration over Cl atom directions with a more restricted subset of directions and enhances the sensitivity of the measurement to alignment effects.

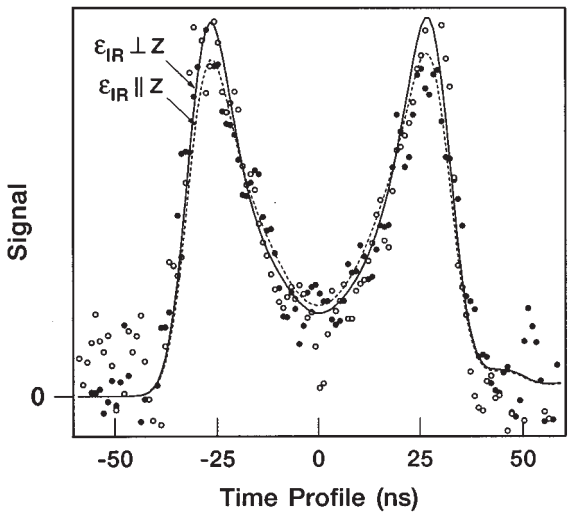

FIG. 18. Cl+$CHD_3(v_1=1, R(1)$ excited) infrared polarization effect for HCl(v=1, J=1). Symbols are as in Fig. 15. Note that the axis alignment of the trideuteromethane excited on this line is similar to that of Fig. 15, whereas the rotational alignment is of the opposite sign.

Because Cl atoms forming HCl(v=1, J=1) are kinematically defined to be at most 20° away from the flight axis, we make the following simplifying assumptions. We take the detection axis as the approach direction of the Cl atom and

we assume a cylindrically symmetric density of reactive Cl atoms about this axis. This assumption of cylindrical symmetry is broken by the polarization of the Cl_2 photolysis, but again because the maximal angle of the Cl from the detection axis that can be possibly detected is small ($<20°$), this symmetry breaking is also small. Note that these assumptions and the assumption that core extraction detects only products parallel to the flight axis systematically lower the measured steric effect from the true effect by a small amount. We estimate this decrease as 20% for the fast products, and we believe this simple treatment is warranted because of its greater transparency over a complete modeling approach. With these assumptions, the reactivity $R_\nu(\omega)$ can then be referenced to the angle of the C–H stretching axis from the laboratory-frame flight axis.

As we have discussed earlier and shown in Appendix B, one-photon infrared excitation of our reagents provides a vibrational alignment in space described by Eq. (3) in which $P_{\mathbf{v}}(\gamma_\nu)$ is the probability of finding the C–H stretching axis at angle γ_ν from ϵ_{ir}. Defining θ_{ir} as the rotation angle from ϵ_{ir} to the flight axis, we rotate the C–H stretching axis alignment into the laboratory-frame flight axis. This rotation of Eq. (3) along with the assumption of cylindrical symmetry (using the azimuthally averaged addition theorem[50]) results in

$$P_{\mathbf{v}}(\omega)=\frac{1+\beta_{\mathrm{axis}}P_2(\cos\ \theta_{\mathrm{ir}})P_2(\cos\ \omega)}{4\pi}. \tag{4}$$

In this formula, β_{axis} describes the magnitude of the axis alignment of the reagent as calculated in Appendix B. This rotated distribution is then multiplied by the reaction probability as a function of ω and integrated over all collisional angles to result in the total signal intensity,

$$\begin{aligned} I&=\int R_{\mathbf{v}}(\omega)P_{\mathbf{v}}(\omega)d\omega \\ &=\frac{1}{4\pi}\left[\int R_{\mathbf{v}}(\omega)d\omega+\beta_{\mathrm{axis}}P_2(\cos\ \theta_{\mathrm{ir}})\right. \\ &\quad\left.\times\int P_2(\cos\ \omega)R_{\mathbf{v}}(\omega)d\omega\right]. \end{aligned} \tag{5}$$

The first term in Eq. (5) is the integral of the reactivity versus approach angle and does not depend on reagent alignment. The second term shows that rotation of the ir polarization can be used to measure the second Legendre moment of the reactivity versus approach angle. These two integrals are our experimental observables. We introduce the following definitions:

$$\frac{I_{\mathrm{iso}}}{3}=\frac{\int R_\nu(\omega)d\omega}{4\pi}. \tag{6}$$

and

$$S^{(2)}=\frac{\int P_2(\cos\ \omega)R_\nu(\omega)d\omega}{\int R_\nu(\omega)d\omega}. \tag{7}$$

Here, $I_{\mathrm{iso}}/3$ is the isotropic rate constant in which the factor of 1/3 is present for normalization, and $S^{(2)}$ is the second Legendre moment of the steric effect. Making these substitutions,

$$I=\frac{1}{3}\,I_{\mathrm{iso}}[1+S^{(2)}\beta_{\mathrm{axis}}P_2(\cos\ \theta_{\mathrm{ir}})]. \tag{8}$$

By measuring the signal I at various angles, θ_{ir}, between the infrared polarization and the flight axis, we can determine the second Legendre moment of the steric effect, $S^{(2)}$, which we will simply refer to hereafter as the steric effect. The simplest measurements are $I_\parallel$ and $I_\perp$, corresponding to $\theta_{\mathrm{ir}}=0°$ and $\theta_{\mathrm{ir}}=90°$, respectively. These definitions result in

$$I_\parallel=\frac{1}{3}\,I_{\mathrm{iso}}(1+S^{(2)}\beta_{\mathrm{axis}}) \tag{9}$$

and

$$I_\perp=\frac{1}{3}\,I_{\mathrm{iso}}\left(1-\frac{1}{2}\,S^{(2)}\beta_{\mathrm{axis}}\right), \tag{10}$$

which can be solved to yield

$$I_{\mathrm{iso}}=I_\parallel+2I_\perp \tag{11}$$

and

$$S^{(2)}\beta_{\mathrm{axis}}=\frac{2(I_\parallel-I_\perp)}{I_{\mathrm{iso}}}. \tag{12}$$

Because the intensity is resolved by its laboratory speed, $I_\parallel$ and $I_\perp$ are time profiles. Therefore,

$$I_{\mathrm{iso}}(t)=I_\parallel(t)+2I_\perp(t) \tag{13}$$

contains the speed distribution, and fitting of the isotropic intensity results in the differential cross section. We use the maximum entropy procedure described in the preceding paper to analyze the data to obtain the differential cross section that is independent of C–H stretch alignment of the reagent molecules. This procedure also results in a fit to $I_{\mathrm{iso}}(t)$. Next, we generate the anisotropy signal

$$I_a(t)=2[I_\parallel(t)-I_\perp(t)]. \tag{14}$$

This signal,

$$I_a(t)=\beta(t)I_{\mathrm{iso}}(t), \tag{15}$$

represents the anisotropic part of the time profiles caused by polarization rotation. $\beta(t)$ is the speed-dependent steric anisotropy; it is the product of the steric effect $S^{(2)}(t)$ and the C–H stretch alignment β_{axis} as shown in Eq. (11). The steric effect can, of course, vary across the differential cross section. As free variation of the anisotropy overdetermines the small difference signals generated by making the combination $I_a(t)$, we bin regions of the differential cross section that have similar scattering to use only a small number of free parameters. For the HCl($v=1$, $J=1$) signal, we use two coefficients, one for the forward-scattered product, and one for the backscattered product. The anisotropy signal is fit by Levenburg–Marquart nonlinear least squares fitting[51] to give the coefficients for each bin. Plots of anisotropy data with this method consist of an isotropic signal $I_{\mathrm{iso}}(t)$ and an anisotropy signal $I_a(t)$ along with their fits. Regions where

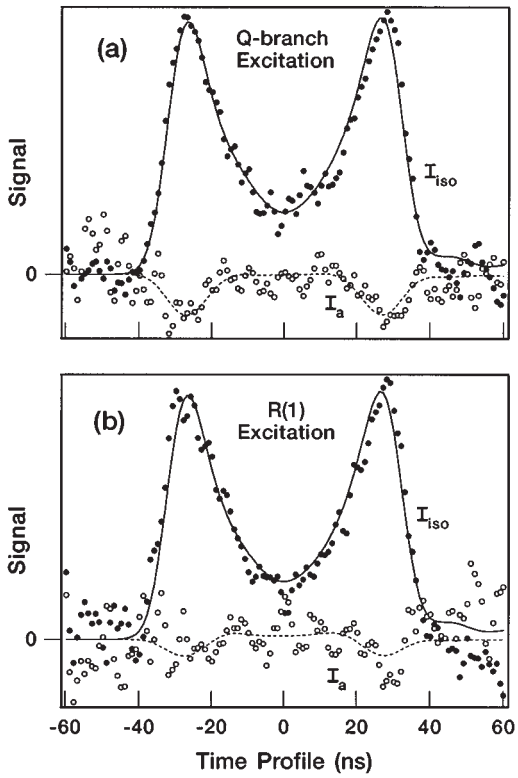

FIG. 19. Cl+$CHD_3(v_1=1)$ steric effects for HCl($v=1$, $J=1$) with either Q-branch excitation, panel (a), or $R(1)$ excitation, panel (b). Both $R(1)$ and Q-branch excitation result in an axial alignment of $\beta_{axis}\approx 0.7$ whereas the rotational alignment changes sign upon branch switching. The solid lines and filled in dots represent the isotropic I_{iso} fits and signals, respectively. They measure the reagent alignment independent differential cross section. The dotted lines and open symbols represent the anisotropy (I_a) fits and signals, respectively. Regions of the signal where I_a is negative correspond to greater reaction at perpendicular geometry than at parallel geometry. The magnitudes of the two signals is such that I_a can vary between -1 and 2 times I_{iso}.

$I_a(t)$ is negative correspond to negative laboratory frame Legendre moments, regions where $I_\perp$ is greater than $I_\parallel$. The signal shown in Fig. 15 can be analyzed in the method described above by generation of the isotropic and anisotropic signals.

Figure 19(a) shows these isotropic and anisotropic signals for the polarization effect for vibrationally excited trideuteromethane as calculated from the data of Fig. 15. These data represent the steric effect for the reaction of Cl with $CHD_3(v_1=1$, Q-branch excitation). Figure 19(b) shows isotropic and anisotropic signals for $R(1)$ excitation of the same reaction (from the raw data of Fig. 18). For Q-branch excitation, β_{axis} is approximately the same as for $R(1)$ excitation. These data are treated quantitatively by analysis of the anisotropy signal. Equation (15) shows that the observed anisotropy signal can be related to the speed-dependent steric anisotropy $\beta(t)$. The steric anisotropy is determined for two bins, one for forward-scattered HCl($v=1$, $J=1$) and one for backscattered HCl($v=1$, $J=1$).

Table I shows these two measured steric anisotropies, β_{fwd} and β_{back}. Because the reaction seldom results in backscattered product, the noise in the backscattered bin is quite large. For this reason, we focus on the β_{fwd} bin for the reaction of Cl with $CHD_3(v_1=1)$. Equation (12) shows that division of the measured alignment effect, β_{fwd}, by the prepared C–H stretch alignment, β_{axis}, results in the normalized second Legendre moment of the probability of reaction versus approach angle, $S^{(2)}_{fwd}$. If our simple vibrational-alignment-only model is correct, $S^{(2)}_{fwd}$ value should not depend on excitation branch, and Table I shows that both measurements of the forward-scattered steric effect are within mutual error bars. The fact that the mean value of the $R(1)$ excitation $S^{(2)}_{fwd}$ is roughly half of the Q-branch excitation value may be caused by miscalculation of the β_{axis} for $R(1)$ excitation. As described in Appendix B, our calculation of β_{axis} neglects nuclear-spin state degeneracies because we do not know the dynamics of CHD_3 cooling in our jet expansion. Our inability to find signal on the $R(0)$ line points to nuclear spin selectivity in our jet, similar to the propensities observed in rotational energy transfer in silane.[52,53] Because Q-branch excitation averages over a number of rotational lines, all of which have similar β_{axis} values, the $S^{(2)}_{fwd}$ value measured by Q-branch excitation is probably more reliable. Rotational alignment also may have some subtle effect on the steric measurement. With these complexities in mind,[54] we conclude that the negative values of the observed anisotropy for both R- and Q-branch excitation are *inconsistent* with a purely rotational effect, and these values imply that C–H stretch alignment dominates rotational alignment in this reaction. In the discussion, we relate the measured $S^{(2)}_{fwd}$ parameter to $R_v(\omega)$ by using Eq. (7).

d. Scattering angle dependence of the steric effect Close examination of Fig. 19 shows that the anisotropy signal is not simply a constant times the isotropic signal. This observation of a changed anisotropy as a function of laboratory speed implies that the steric effect changes with scattering angle. Although this effect is difficult to see because of the poor signal-to-noise ratio in the backscattered region, it is

TABLE I. Fitted anisotropy parameters for the reaction Cl+$CHD_3(v_1=1)\rightarrow$HCl($v=1$, $J=1$)+CD_3.

Excitation	β_{axis}	β_{fwd}[a]	β_{back}[a]	$S^{(2)}_{fwd}$	$S^{(2)}_{back}$
Q branch	$\sim+0.7$[b]	-0.17 ± 0.06	$+0.39\pm0.33$	-0.24 ± 0.08	$+0.56\pm0.47$
$R(1)$	$\sim+0.7$	-0.07 ± 0.06	$+0.33\pm0.33$	-0.11 ± 0.10	$+0.47\pm0.47$

[a]The forward- and backscattered regions are defined by dividing the scattering at the speed of the center of mass. All products moving faster than the center of mass are included in the forward-scattered bin and all products slower than the center of mass are included in the backscattered bin.

[b]Q-branch axis alignment and rotational alignment are estimated by weighted summation of the axis and rotational alignments with our best estimate of the populations excited by pumping on the Q branch.

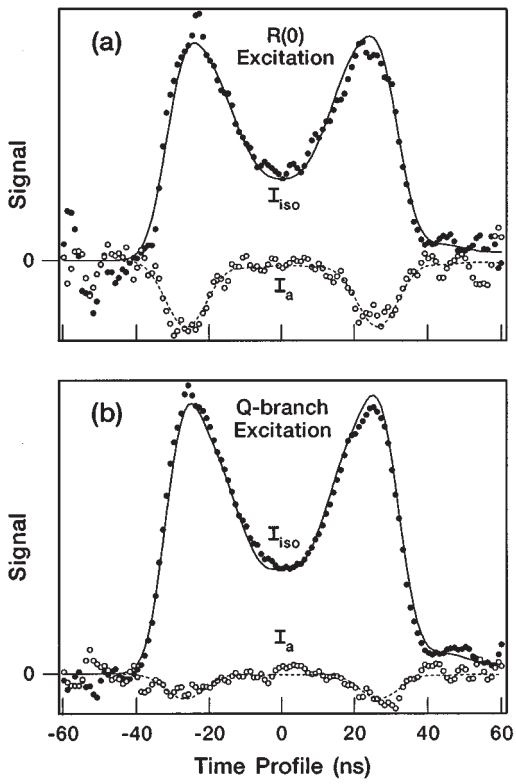

FIG. 20. $Cl+CH_4(v_3=1)$ steric effect for $HCl(v=1, J=1)$. Panel (a) shows the isotropic and anisotropic signals for $R(0)$ excitation, and panel (b) shows the results for Q-branch excitation. The $R(0)$ vibrational amplitude alignment is $\beta_{axis}=2$ on the $R(0)$ line and $\beta_{axis}\approx 0.7$ on the Q branch. Lines and symbols are as in Fig. 19.

indicated by our modeling, which required two anisotropy parameters, β_{fwd} and β_{back}, to effectively fit the data. Results for the reaction of Cl with $CH_4(v_3=1)$ also support this conclusion (discussed in the next sections). The observed effect seems to show an anisotropy signal that is less negative in the slower velocities, implying that the steric effect becomes more positive for the backscattered $HCl(v=1, J=1)$ products. Although some of this effect may arise from imperfect core extraction, as discussed later, the scattering angle dependence of the steric effect seems to show that while the forward-scattered $HCl(v=1, J=1)$ product is enhanced in collisions in which the stretch-excited C–H bond is perpendicular to the approach direction of the chlorine atom, this enhancement by perpendicular collision is diminished for the backscattered product.

2. $Cl+CH_4(v_3=1)$

Investigation of the excitation polarization dependence for the reaction of atomic chlorine with vibrationally excited methane points to strong parallels between this reaction and that of vibrationally excited CHD_3. Figure 20(a) shows the isotropic and anisotropic signals for the reaction of Cl with $CH_4(v_3=1, J=1)$ excited on the $R(0)$ line as derived by the methods described above from excitation polarization dependent time-profile measurements. Figure 20(b) shows isotropic and anisotropic signals from Q-branch excitation of the same reaction. Because the alignment of the angular momentum always changes upon branch switching, the negative anisotropy measured on both excitation branches points once again to a vibrational alignment effect. Excitation of $CHD_3(v_3=1)$ on $R(0)$ results in a C–H stretch alignment approximately three times stronger than Q-branch excitation, which implies that if we could have found reactive signal on the $R(0)$ branch for that reaction, its anisotropy would have been three times stronger than Q-branch excitation anisotropy. Figure 20 shows a ratio of approximately three times stronger anisotropy effect for $R(0)$ versus Q-branch excitation in the vibrationally excited methane reaction, which indicates that vibrationally excited methane and trideuteromethane seem to be reacting quite similarly.

Observation of any anisotropy in the reaction of atomic chlorine with vibrationally excited methane may regarded by some as surprising. Because HCl product can result from collision of Cl with any of the four H atoms on $CH_4(v_3=1)$, an alignment effect implies that some hydrogen atoms are more reactive than others in $CH_4(v_3=1)$ and that collision does not scramble this difference. Facile scrambling might be expected because all the C–H oscillations have identical bond strengths and force constants, which could allow scrambling of the localization that leads to the steric effect without energy mismatch in the vibrational mode mixing. This collision-induced mode mixing effect has important implications for mode- or bond-specific chemistry because it would tend to wash out mode-specific vibrational effects. In typical bond-specific chemistry experiments, the reactivity of two oscillators with *distinct* vibrational frequencies is controlled by excitation of either of these (possibly local) modes. In those experiments, the vibrational energy mismatch between the oscillators is likely to suppress collision-induced mode mixing. This energy mismatch might have contributed to the mode-specific behavior we have observed in the $Cl+CHD_3(v_1=1)$ reaction. For $Cl+CH_4(v_3=1)$, the lack of such an energy mismatch might be expected to destroy the energy localization. We observe, however, a strong effect for $Cl+CH_4(v_3=1)$ in which C–H bonds are not equivalent in all spatial directions. Therefore, collision-induced mode mixing must not be strong in the $Cl+CH_4$ system.

a. Polarization of $CH_4(v_3=1)$ resulting from excitation. Infrared excitation of the methane molecule polarizes its vibrational amplitude. This alignment is caused by the $|\mu\cdot\epsilon_{ir}|^2$ term in the interaction of the infrared light with the molecule, just as for $CHD_3(v_1=1)$. The ν_3 mode of methane is a triply degenerate vibration, complicating the calculation of alignment of the vibrationally excited molecule. Because the angular momentum alignment does not depend on the mode excited, our previous calculation of rotational alignment of $CHD_3(v_1=1)$ applies to the methane molecule. Therefore, Fig. 16 represents the alignment of the total angular momentum of the methane molecule following infrared excitation. Unlike $CHD_3(v_1=1)$, however, this total angular momentum is not simply the rotation of the molecule in space. For $v_3=1$ methane, the degenerate vibrational motions lead to vibrational angular momentum, denoted by **l**. The total angular momentum, **J**, is the vector summation of **N**, the rotational angular momentum, and **l** ($l=1$ for $v_3=1$), hence

TABLE II. Fitted anisotropy parameters for the reaction $Cl+CH_4(v_3=1)\rightarrow HCl(v=1, J=1)+CH_3$.

Excitation	β_{axis}	β_{fwd}[a]	β_{back}[a]	$S^{(2)}_{fwd}$	$S^{(2)}_{back}$
$R(0)$	$+2$	-0.38 ± 0.03	$+0.11\pm0.12$	-0.19 ± 0.02	$+0.06\pm0.06$
Q branch	$\sim+0.7$[b]	-0.11 ± 0.02	$+0.09\pm0.06$	-0.15 ± 0.02	$+0.12\pm0.09$

[a]The forward- and backscattered regions are defined by dividing the scattering at the speed of the center of mass. All products moving faster than the center of mass are included in the forward-scattered bin and all products slower than the center of mass are included in the backscattered bin.
[b]Q-branch axis alignment is assumed to be the same as for $CHD_3(v_1=1)$.

$\mathbf{J}=\mathbf{N}+\mathbf{l}$.[55,56] The vibrational angular momentum has a projection k_l onto the body-fixed axis of the methane molecule. The state with $k_l=0$ corresponds to vibration parallel to the body-fixed axis, whereas the states with $k_l=\pm1$ correspond to perpendicular vibration.[57] Therefore, polarization of the vibrational angular momentum corresponds to polarization of the vibration of the methane molecule.

The selection rules for infrared absorption imply that strong transitions have $\Delta N=0$ in addition to the usual $\Delta J=0,\pm1$;[55,56] thus excitation of CH_4 on the $R(0)$ line results in a molecule with $J=1$, $l=1$, and $N=0$. Because $N=0$, this molecule has no physical rotation, and its angular momentum polarization corresponds purely to a polarization of the vibrational angular momentum, which in turn corresponds to a polarization of the vibration in space. Following $R(0)$ excitation, the probability of finding the vibrational axis in laboratory space is described by Eq. (3) with $\beta_{axis}=2$. Because this state is rotationless, any orientation of the methane hydrogen atoms is equally likely, yet the vibrational axis is polarized. A classical model of this behavior views the vibrating methane molecule as a vibrating ellipse in which the excited axis is polarized in space and the hydrogen atoms are located on this elliptical surface with some unknown orientation. Calculating the alignment of the vibrational amplitude for other states is beyond the scope of this paper, but because the interaction with polarized light leading to $CH_4(v_3=1)$ vibrational axis alignment is the same as for C–H stretch alignment in $CHD_3(v_1=1)$, the excitation branch dependence should be similar.

To search for rotational effects in the reaction of chlorine with vibrationally excited methane, we recorded ''high resolution'' time profiles at fixed ir polarization on various excitation rotational branches and lines. This study showed effects weaker than the vibrational effects shown here and were observable only because of the high resolution of the measurement associated with the larger signal for $Cl+CH_4(v_3=1)$ than for $Cl+CHD_3(v_1=1)$. These effects are small and complicated to analyze because they arise from both rotationally and vibrationally aligned molecules. These results are described in Appendix C. The vibrational effect for $CHD_3(v_1=1)$ showed perpendicular collisions lead to increased forward-scattered product. In the reaction of $CH_4(v_3=1)$, we observe that collisions in which the atomic chlorine approaches perpendicular to the polarized vibrational amplitude of methane lead to increased forward scattering. Therefore, by analogy, we can identify the more reactive hydrogen atoms in vibrationally excited methane as the hydrogen atoms parallel to the vibrational amplitude. Collisionally induced mode mixing discussed earlier may decrease the steric effect, but the strong magnitude of the observed steric effect seems to indicate that such mixing is weak.

b. Scattering angle dependence of the steric effect. In the reaction of atomic chlorine with vibrationally excited trideuteromethane, we observed that the steric anisotropy signal varied as a function of the scattering angle. For the reaction of atomic chlorine with vibrationally excited methane, this effect is again observed. The increased signal of the vibrationally excited methane reaction along with the stronger axis alignment provided by $R(0)$ excitation helps us to observe this effect more clearly. In Fig. 20, we see that the anisotropy signal is fairly close to zero for the backscattered $HCl(v=1, J=1)$, which appears near ±15 ns, but strongly negative for the forward-scattered $HCl(v=1, J=1)$, which appears near ±30 ns. Therefore, the steric effect in this reaction, just as for the $Cl+CHD_3(v_1=1)$ reaction, changes with the scattering angle. Specifically, the $S^{(2)}$ value becomes more positive in the backscattered region. Although the experimental anisotropy signal does not show a significantly positive region, the inward trailing of the faster functions must be negated by a positive anisotropy parameter to fit the experimental data. Table II shows the deconvoluted steric effects for the forward- and backscattered regions. $S^{(2)}_{back}$ is positive, which implies that this backscattered product results from reactions in which the vibrational amplitude is polarized parallel to the approach direction of the chlorine atom in preference to perpendicular collisions. We note that there is an implicit assumption of perfect core extraction in this simple analysis method. While we know that the core extraction is degraded for slow products, we do not know how much this affects the observed anisotropy signal. Therefore, we believe that the data indicate a change in the steric effect, but do not quantitatively believe the $S^{(2)}_{back}$ fitting parameter. Again, excitation branch switching indicates that the effect is consistent with pure vibrational alignment and inconsistent with pure rotational alignment.

IV. DISCUSSION AND CONCLUSIONS

Using the core-extraction technique, we have investigated the related photoinitiated reactions of Cl with $CH_4(v_3=1)$ and $CHD_3(v_1=1)$. We were able to obtain state-to-state differential cross sections for essentially all populated rotational levels in both accessible vibrational states of the HCl product. The $HCl(v=1,J)$ product shows a cold rotational distribution; approximately 30% of the product ap-

pears in this vibrational state. This vibrational state shows predominantly forward scattering at all observed rotational states, and backscattering grows to rival the forward-scattered peak by $J=3$. The HCl($v=0,J$) product shows a warmer rotational distribution with back- and side-scattered product in coincidence with low methyl vibrational excitation. We see that there are strong differences in the angular distributions not only between HCl($v=0$) and HCl($v=1$) but also between the different rotational levels of the same vibrational state. In addition, we aligned the C–H stretch of the vibrationally excited methanes using linearly polarized ir excitation and recorded how this alignment affects reactivity. By these means, we put forward a detailed picture of how a chlorine atom abstracts hydrogen from vibrationally excited methane.

The reactions of atomic chlorine with vibrationally excited CH_4 and vibrationally excited CHD_3 show similar state and scattering distributions, which implies that the reactivity is mostly that of the excited C–H bond and depends weakly on the symmetry of the reagent. The only significantly changed observable when comparing $Cl+CHD_3(v_1=1)$ and $Cl+CH_4(v_3=1)$ is the vibrational branching ratio, which is about a factor of 2 smaller for the former reaction. Somehow, the presence of a deuteromethyl radical instead of a methyl radical changes the vibrational branching ratio. We are uncertain of the origin of this change. The simple models presented here essentially take methane to be methyl-hydride and therefore are not able to explain this change. It is possible that the increased density of states of the methyl-d_3 radical as compared to the methyl radical weakens the vibrational adiabaticity. The change in vibrational branching ratio could also be some effect of differences of the C–H motions in $CHD_3(v_1=1)$ compared to $CH_4(v_3=1)$, or some quantum mechanical effect.

These measurements of the reaction of atomic chlorine with vibrationally excited methane provide evidence that multiple reaction mechanisms operate to give distinct hydrogen chloride products. The differential cross section for HCl($v=1$) changes with rotational state, shifting toward backscattering as the rotational quantum number increases. We previously observed this effect at low resolution by non-core-extracted measurements of the speed distribution.[11] A model in which two mechanisms produce HCl($v=1$) was developed to explain these observations. In this model, the dominant mechanism corresponds to reaction of Cl with a peripheral H atom on the $CH_4(v_3=1)$ molecule. This dominance results in forward-scattered product with a cold rotational state distribution. Because the HCl product in $v=1$ moves at nearly the same speed and direction as the approaching Cl atom, there should be little impulsive kick on the product, resulting in low rotational excitation. Collisions that backscatter require an impulsive kick to redirect their initial velocity and should be more rotationally excited. In our previous publication,[11] we interpreted the fact that the HCl($v=1$) higher J product is more backscattered as evidence for this pathway.

In the present study we observe the HCl($v=0,J$) product of this reaction and find it to be back and side scattered and rotationally excited. Our observations of the speed distribution and spatial anisotropy of HCl($v=0,J$) demonstrate that the exothermicity of this channel becomes converted largely into translation, leaving the methyl radical with little to no vibrational energy. For a direct reaction, little excitation is expected to be deposited in ''spectator bonds,'' that is, bonds neither made nor broken in the reaction. The observation of low excitation of the methyl fragment agrees with this expectation for the spectator methyl group and also with the conventional view that originates from the studies of the reaction of O(^3P) and Cl(^2P) with hydrocarbons,[12,14–17] in which the nature of the hydrocarbon radical was thought to be unimportant. A cold methyl vibrational distribution like that observed by Suzuki and Hirota[58] in the reaction of atomic oxygen (O^3P and O^1D) with methane fits our experimental anisotropy measurement very well, pointing to similarities in these reactions. Because the methyl radical consumes little of the exothermicity, the HCl($v=0,J$) product experiences an impulsive kick, forcing it to recoil from the center of mass with a speed greater than the chlorine atom approached in the center-of-mass frame. This impulsive release into the HCl($v=0,J$) product is likely to excite rotation, as is observed experimentally. Additionally, we would expect the impulse to be in the direction of the C–H bond broken at the transition state. If the transition state does not rotate significantly, the C–H bond must be on the hemisphere pointing backwards toward the Cl atom approach direction. This situation implies that the impulse should push the HCl($v=0,J$) sideways or backwards for this exothermic pathway, leading to side- and backscattered HCl($v=0,J$), again in agreement with the experimental observations.

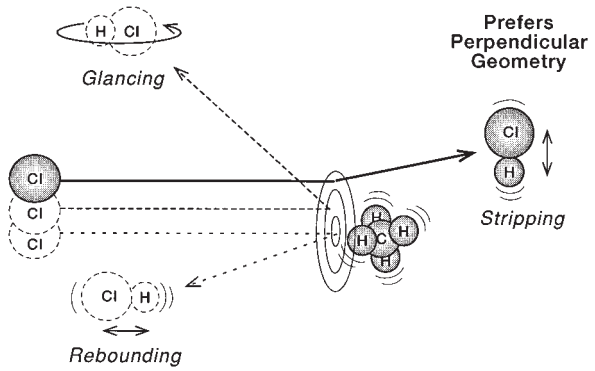

FIG. 21. Model for the observed scattering behavior of atomic chlorine reacting with vibrationally excited methane.

Figure 21 schematically illustrates these ideas of the competition between different reaction mechanisms in the reaction of atomic chlorine with vibrationally excited methane. The backscattered HCl($v=0,J$) and rotationally excited HCl($v=1$) pathways correspond to a predominantly linear transition state formed by the collinear nature of the potential surface and rotational excitation originating from impulsive release of the bent transition state. Vibrational excitation has been predicted to open the range of reactive impact parameters, or equivalently, the cone of acceptance, by localizing energy in the correct motion for reaction and lessening the requirement for line-of-centers energy,[2] allowing peripheral

reaction.[59] We propose that the vibrational excitation of the methane molecule leads to the observed scattering behavior by allowing reaction at large impact parameters. These large impact parameter collisions then lead to the forward-scattered rotationally cold HCl(v=1). In this model, the impact parameter determines where the product scatters and how the excess energy is partitioned between translation, rotation, and vibration. As will be seen in the following discussion, the dependence of the reactivity on the approach direction of the Cl atom to the C–H stretch vibration provides confirming evidence for the validity of the model we have presented here.

Our overall picture of the alignment effects in the reaction of atomic chlorine with vibrationally excited methane is one of a reaction dominated by C–H vibration and secondarily affected by methane rotation. The experiment measures the expectation value of the second Legendre moment of the probability of reaction versus approach angle. The theoretically possible range of the steric effect is $-0.5 \leqslant S^{(2)} \leqslant +1.0$. The Q-branch excitation steric effect measurement for forward-scattered HCl(v=1, J=1) from the Cl+CHD_3(v_1=1) reaction results in $S^{(2)}_{\mathrm{fwd}} \approx -0.2$, a value nearly half the maximum perpendicular steric effect. This steric effect is quite close to that derived from the reaction Cl+CH_4(v_3=1), indicating that collision-induced mode mixing is probably negligible. Therefore, a steric effect for forward-scattered HCl(v=1, J=1) of $S^{(2)}_{\mathrm{fwd}} \approx -0.2$ is indicative of the steric requirements for this channel in the reaction of Cl with C–H stretch excited methane and trideuteromethane.

A few simple models for the form of this reactivity versus angle help give a feel for some of the distributions that are consistent with our steric measurement. The simplest form of $R_{\mathbf{v}}(\omega)$ is a delta function, which implies that all reaction occurs at a single angle. In this fairly unrealistic case, the measured $S^{(2)}_{\mathrm{fwd}} \approx -0.2$ value for the forward-scattered HCl(v=1, J=1) product from the reactions of atomic chlorine with vibrationally excited trideuteromethane and methane can be inverted by the equation $S^{(2)} = \langle P_2(\cos \omega_\delta) \rangle = P_2(\cos \omega_\delta)$, which results in an angle ω_δ of 63°. A more realistic model would take a band of constant reactivity starting at some angle ω_c and continuing to the end of the front hemisphere of the methane molecule. This model is described by the function $R_{\mathbf{v}}(\omega)=0$ for $\omega < \omega_c$ and $R_{\mathbf{v}}(\omega)$=constant for $\omega_c \leqslant \omega < 90°$. This model results in an $S^{(2)}$ value of $S^{(2)} = \langle P_2(\cos \omega) R_{\mathbf{v}}(\omega) \rangle = -\sin^2 \omega_c/2$, which implies that the data are consistent with a constant reactivity from 39° to 90° and no reactivity from 0° to 39°. Note that the mean angle of these two distributions is similar, therefore, our data point to a distribution with ill-determined width but a mean somewhere near 65°. These models demonstrate two possible steric effects consistent with our data and aid us in picturing the collisional geometries responsible for these effects. The fact that the measured steric effect for the forward-scattered component of the HCl(v=1, J=1) is negative inescapably points to T-shaped transition-state geometries as being preferentially responsible for forward scattering of HCl(v=1, J=1).

The data also demonstrate that the steric effect changes as a function of the scattering angle. While some of this effect may arise from imperfect core extraction, the data show a more positive $S^{(2)}$ value for backscattered HCl(v=1, J=1) than for the forward-scattered product, implying a weaker preference for perpendicular collisional geometries. Additionally, the observation of steric effects in the reaction of atomic chlorine with vibrationally excited methane, CH_4(v_3=1), implies that the vibrational energy initially polarized preferentially parallel to the electric vector of the excitation is not severely collisionally scrambled during the reaction. Steric effect measurements show that the forward-scattering mechanism of the HCl(v=1) product results from peripheral collision geometries, reinforcing the model presented in Fig. 21. These dynamics may be caused by reaction on a part of the potential energy surface where the barrier to reaction does not increase sharply with bend angle of the transition state. We proposed that this region of the potential energy surface is sampled because vibrational excitation of methane opens the cone of acceptance and lessens the requirement for transition state linearity.

The core-extraction technique has permitted us to study the photoinitiated bimolecular reactions Cl($^2P_{3/2}$)+CH_4(v_3=1) and Cl($^2P_{3/2}$)+CHD_3(v_1=1) to an unprecedented level of detail. In particular, we have observed that the angular-scattering distribution can completely change with small changes in internal state. Moreover, the core-extraction method along with polarized ir state-preparation of reagents allows us to measure the dependence of the reactivity on the vibrational and rotational alignment through its power to distinguish products by internal state and by scattering. By these means, we have come closer to achieving the goal of specifying in sufficient detail the measurable attributes of a reactive collision so that we can develop a deep understanding of chemical change.

ACKNOWLEDGMENTS

S.A.K. and W.R.S. thank the National Science Foundation for predoctoral fellowships. This work has been supported by the National Science Foundation under Grant No. CHE-93-22690.

APPENDIX A: ROTATIONAL POPULATION CORRECTION FACTORS

Integral ion signals for HCl(v=1,J) were measured via the Q-branch lines of the E–X (0,1) transition. To convert these signals to populations, we used the correction factors of Rohlfing, Chandler, and Parker,[41] who measured mass-integrated ion signals from a 300 K HCl(v=1) population for each line. Because ionization on this electronic state produces molecular (HCl^+), hydrogen (H^+), and chlorine (Cl^+) ions, a branching ratio is required. Although Rohlfing *et al.* observed a constant branching into each of the observed product ions, we have observed variations of these branching ratios for different rotational lines. Possibly some change in ionization laser focusing conditions is responsible for this slight discrepancy. We have measured the fragmentation branching ratio and applied our measured branching ratios to the mass-integrated correction factors of Rohlfing *et al.*[41] to

TABLE III. HCl $E-X$ (0,1) REMPI correction factors.

J	$C(Q$ branch)[a]
0	1.00
1	0.65
2	0.65
3	0.63
4	0.54

[a]Correction factors for H^+ ion detection including fragmentation.

obtain a set of correction factors for H^+ ion signals on the $E-X$ (0,1) band Q branch. Note that the only significant variation of fragment ion branching occurs for the $Q(0)$ line. These factors are listed in Table III. The final correction factors are used to calculate populations from H^+ detected ion signals by the formula

$$N = C(\text{branch},J)S, \tag{A1}$$

where N is the population, S is the signal, and $C(\text{branch},J)$ is the correction factor. Because the laser power variation was insignificant over the small scan range of the $E-X$ (0,1) Q branch, no power correction was applied. Our measurements of the fragmentation process seem to indicate that it is power dependent; therefore, we caution that the correction factors presented here may not apply to experiments performed under different ionization conditions.

Rotational correction factors for the $F-X$ (0,0) and $F-X$ (1,1) diagonal bands were calculated by correcting two-photon linestrengths[60] for predissociation of the intermediate state. The state-dependent predissociation was measured by Gordon and co-workers.[37,61] The result of this calculation is two sets of rotational correction factors, one for $v=0$ and one for $v=1$. The power dependence was measured on a number of rotational lines and found to be quadratic within error bars. Because a quadratic power dependence is predicted for this 2+1 REMPI process, P^2 was used for power normalization where P is the laser power

$$N = C(\text{branch},J)\,\frac{S}{P^2}. \tag{A2}$$

The rotational correction factors were scaled with respect to each other by measurement of a vibrational correction factor. The vibrational correction factor was measured by tuning the infrared laser to excite HCl to $v=1$ on various rotational lines and then by ionizing both the HCl($v=0$) level depleted by the infrared excitation and the HCl($v=1$) level enhanced by the ir on the $F-X$ (0,0) and (1,1) bands. Because the depleted population appears in the enhanced spectrum, a ratio of the enhancement signal to the depletion signal can be used with the rotational correction factors described above to determine a vibrational correction factor. These vibrational and rotational correction factors are used to calculate a set of rovibronic correction factors listed in Tables IV and V. These factors use the same formula, Eq. (A2), to convert signal to population. Notice that the F-state correction factors allow determination of vibrational branching but are arbitrarily normalized with respect to the E-state $v=1$ correction factors.

TABLE IV. HCl $F-X$ (0,0) REMPI correction factors.

J	$C(R,(0,0))$	$C(S,(0,0))$
0	a	0.67
1	1.00	1.88
2	1.57	3.48
3	2.44	5.13
4	3.30	7.82
5	4.78	9.05
6	5.35	9.97
7	5.75	6.37
8	3.612	b
9	b	4.32
10	2.39	5.56

[a]Line does not exist because of the symmetry of $F\ ^1\Delta_2$ state.
[b]Perturbation coefficient is not available for $F\ ^1\Delta_2$ ($v=0$, $J=10$); therefore, $R(9)$ and $S(8)$ correction factors were not calculated.

APPENDIX B: CALCULATIONS OF ALIGNMENT FOLLOWING IR EXCITATION

Zare[46] calculates the alignment of the total angular momentum resulting from one-photon ir absorption. The total angular momentum alignment parameter, $A_0^{(2)}$, is given by

$$A_0^{(2)} = \begin{cases} -\dfrac{2}{5} + \dfrac{3}{5(J_f+1)} & P(J_f+1)\ \text{excitation}, \\ +\dfrac{4}{5} - \dfrac{3}{5J_f(J_f+1)} & Q(J_f)\ \text{excitation}, \\ -\dfrac{2}{5} - \dfrac{3}{5J_f} & R(J_f-1)\ \text{excitation}. \end{cases} \tag{B1}$$

Note that the formula for $P(J_f+1)$ excitation shown above is incorrect for $J_f=0$, which is caused by division by zero that is not apparent after simplification. $P(1)$ excitation prepares $J_f=0$ and therefore must result in $A_0^{(2)}=0$. The values of $A_0^{(2)}$ as a function of J_f are plotted in Fig. 16.

The degree of bond alignment versus excitation branch and prepared rotational level was also calculated by Zare[46] but for the specific case of a linear molecule. In the case of trideuteromethane, we excite molecules without resolution of the K quantum number. Consequently, our alignment is slightly different from the previously calculated alignment.

TABLE V. HCl $F-X$ (1,1) REMPI correction factors.

J	$C(Q,(1,1))$	$C(R,(1,1))$	$C(S,(1,1))$
0	a	a	1.11
1	a	1.67[b]	3.07
2	3.89	2.56	3.83
3	3.84	2.68	4.06
4	3.28	2.61	5.20
5	2.83	3.18	6.57
6	3.18	3.88	

[a]Line does not exist because of the symmetry of $F\ ^1\Delta_2$ state.
[b]These correction factors were scaled with respect to the $F-X$ (0,0) by application of a vibrational correction factor. This factor is the ratio of signal on $R(1)$ for the (0,0) and (1,1) bands of the $F-X$ transition. The ratio was measured to be $v=1/v=0=1.67\pm0.42$ ($\pm2\sigma$). All other correction factors were scaled accordingly.

The K quantum number describes the projection of **J** onto the top axis. For trideuteromethane, the top axis corresponds to the C–H bond direction. Excitation of the ν_1 mode is a parallel band and has the selection rules $\Delta J=0,\pm 1$ and $\Delta K=0$ provided that $\Delta J\neq 0$ when $K=0$.[32] With these selection rules and at the resolution of our infrared laser (approximately 1 cm^{-1}), a diatomiclike structure appears where all K values are simultaneously excited in stacks that are labeled Q_R, Q_Q, and Q_P for $\Delta J=+1$, 0, and -1, respectively. The superscript Q represents the ΔK quantum number, which is always 0 for this parallel band. The probability of exciting the state $|J_iK_iM_i\rangle$ for linearly polarized light is given by

$$P(J_i,K_i,M_i,J_f,K_f,M_f) = S_{\mathrm{tr}}\left|\begin{pmatrix} J_i & 1 & J_f \\ M_i & 0 & -M_f \end{pmatrix}\right|^2 \left|\begin{pmatrix} J_i & 1 & J_f \\ K_i & 0 & -K_f \end{pmatrix}\right|^2, \tag{B2}$$

where S_{tr} is a constant dependent on the transition. We take the symmetric top to be unpolarized before excitation, i.e., all M and K states are taken to be equally populated.

As mentioned earlier, the angular distribution of axes after excitation is of the form

$$P(\gamma)=\frac{1+\beta_{\mathrm{axis}}P_2(\cos\gamma)}{4\pi}, \tag{B3}$$

where β_{axis} is dependent on the rotational line used to excite the molecule and γ is the angle of the top axis from the quantization axis. For a pure $|JKM\rangle$ state, the probability of finding the top axis at an angle γ from the quantization axis (the electric vector of the polarized light) is given by the equation (Zare, p. 123)[50]

$$P_{JKM}(\gamma)=(-1)^{M-K}\frac{2J+1}{2}\sum_{n=0}^{2J}(2n+1)\begin{pmatrix} J & J & n \\ M & -M & 0 \end{pmatrix}\times\begin{pmatrix} J & J & n \\ K & -K & 0 \end{pmatrix}P_n(\cos\gamma). \tag{B4}$$

We need concern ourselves only with the $n=0$ and $n=2$ terms of this expansion to calculate β_{axis}. The $n=0$ term is 1/2. Therefore, we find that β_{axis} equals twice the $n=2$ term of this expansion. Inserting analytical expressions for the 3-j symbols, we find

$$\beta_{\mathrm{axis}}=\sum_K P(K)\sum_M P(M)\times\frac{5(3M^2-J(J+1))(3K^2-J(J+1))}{J(J+1)(2J+3)(2J-1)}, \tag{B5}$$

where $P(M)$ and $P(K)$ are the normalized probabilities for the state to make the projections M and K. This expression can be separated into two parts, one for M and one for K

$$\beta_{\mathrm{axis}}=\sum_M P(M)\frac{3M^2-J(J+1)}{J(J+1)}\times\sum_K P(K)\frac{5(3K^2-J(J+1))}{(2J+3)(2J-1)}. \tag{B6}$$

The first summation is recognized as equal to the $A_0^{(2)}$ moment for the excitation branch. In our case, the limited resolution of the infrared laser is insufficient to resolve individual K states under the K stacks, so we excite all K values based only on their line strengths. Inspection of the 3-j symbol for the K part of the line strength shows that it is of the exact same form as the M part; thus the K summation can also be related to $A_0^{(2)}$ in the case of unresolved K structure

$$\beta_{\mathrm{axis}}=A_0^{(2)}\frac{5J(J+1)}{(2J+3)(2J-1)}\times\sum_K P(K)\frac{(3K^2-J(J+1))}{J(J+1)}, \tag{B7}$$

$$=(A_0^{(2)})^2\frac{5J(J+1)}{(2J+3)(2J-1)}.$$

This calculation, while instructional, is not exactly correct for our case because we have neglected the nuclear spin states of trideuteromethane and our reagent preparation process. The three deuterons in CHD_3 lead to degeneracies for the JK states, which in turn lead to population alternations in a thermal sample. This indistinguishability of the deuterium atoms breaks the assumption of equal populations of K states, which allowed us to arrive at the simple form for the axis alignment. Unfortunately, in our case the problem is even more complex because we rotationally cool our reagent CHD_3 molecules to concentrate them in the lower states, thereby increasing the number density of molecules able to absorb the infrared radiation and become vibrationally excited. This cooling process is nonthermal and has very interesting propensities for fine-structure-resolved rotational energy transfer, as observed by Steinfeld and co-workers[52,53] in silane and explained by the theory of Parson.[62,63] Because we do not know the rotational temperature of our reagents, or even whether a temperature effectively describes the population distribution, we are not able to make an exact calculation of the bond axis alignment. In the absence of further knowledge about the nature of our expansion, we use the numbers calculated above as approximate values for the bond axis alignment. We also note that the $R(0)$ alignment is correct because the starting state of this branch is nondegenerate.

APPENDIX C: METHANE ROTATIONAL ALIGNMENT EFFECTS

By examining high-resolution core-extracted time profiles at fixed ir polarization, we were able to detect a weak effect ascribable to rotational state alignment. Figure 22 shows core-extracted time profiles for HCl(v=1, J=1) from the reaction of atomic chlorine with vibrationally excited methane in (a) $J=1$ prepared on the $R(0)$ excitation line; (b) $J=3$ prepared on the $R(2)$ excitation line; and (c) a mix of

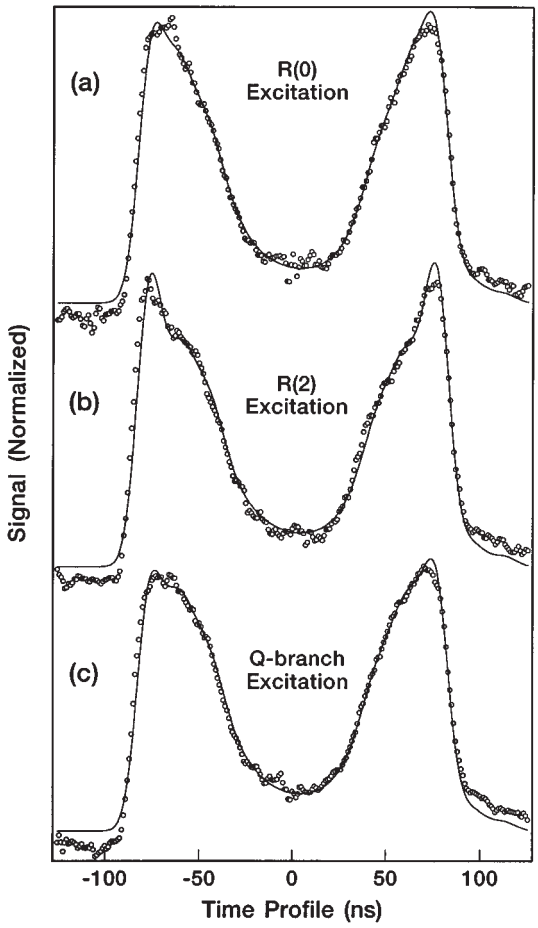

FIG. 22. Core-extracted time profiles for HCl(v=1, J=1) recorded by varying the rotational state of methane and branch of excitation. These data are taken with fixed polarization of infrared light perpendicular to the flight axis, which preferentially samples perpendicular collisional geometries. (a) CH_4(v_3=1, J=1) reagent prepared on the $R(0)$ line. (b) CH_4(v_3=1, J=3) reagent prepared on the $R(2)$ line. (c) CH_4(v_3=1, J=1 to ~3) reagent prepared on the Q branch. The signals are offset vertically for clarity.

$J=1$ to $J\approx 3$ prepared by excitation on the Q branch. The linear polarization of the infrared laser was perpendicular to the flight axis, and the time profiles shown in Fig. 22 were recorded by tuning the ir laser between various excitation lines. Because the vibrational axis alignment follows the ir polarization, collisions of atomic chlorine perpendicular to the vibrational amplitude of methane are preferentially sampled in all three panels of this figure.

Although we are not sure of the exact nature of the rotational states of methane present in our expansion, we can measure reactive signal while exciting methane on the R branch to estimate which states are populated. Assuming that the integral reaction cross section into HCl(v=1, J=1) does not strongly vary with rotational state, this measurement provides an estimate of the populations of the methane molecules in our expansion after jet cooling. We find comparable reactive signal for excitation of methane on $R(0)$, $R(1)$, and $R(2)$, with less on $R(3)$ and only a small amount on $R(4)$, which indicates the rotational temperature of the methane molecules in the expansion is near 0 K. Hence, we identify the Q branch as primarily $J=1$ to $J=3$; note that $Q(0)$ does not exist.

Despite the similarity of the Q-branch excitation data and the $R(0)$ excitation data, the reaction for $R(2)$ excitation shows a slight increase in the sharpness of the forward-scattered peak, as evidenced by the inflection just inside the outer peaks of the symmetric time profile. This sharpening of the forward scattering is also visible for reaction of methane following $R(3)$ and $R(1)$ excitation (data not shown). This rotational effect is clearly weak, but possibly the tumbling motion of methane molecules prepared on $R(2)$, which results from the preference for rotation perpendicular to the axis alignment, leads to enhanced forward scattering by causing the hydrogen atoms to track along with the stripping Cl motion. In this model, no enhanced stripping is seen because the rotation excited on the Q branch is preferentially parallel to its vibrational amplitude. Recall that $R(0)$ excitation in methane has no rotation of the molecule; therefore, methane excited on $R(0)$ also cannot track the Cl stripping motion. This weak effect may also be related somehow to more subtle combinations of vibration and rotation of this highly degenerate molecule.

[1] G. W. Flynn and R. E. Weston, Jr., Annu. Rev. Phys. Chem. **37**, 551 (1986).
[2] R. D. Levine and R. B. Bernstein, *Molecular Reaction Dynamics and Chemical Reactivity* (Oxford University, New York, 1987).
[3] D. A. V. Kliner and R. N. Zare, J. Chem. Phys. **92**, 2107 (1990).
[4] D. E. Adelman, N. E. Shafer, D. A. V. Kliner, and R. N. Zare, J. Chem. Phys. **97**, 7323 (1992).
[5] M. J. Bronikowski, W. R. Simpson, and R. N. Zare, J. Phys. Chem. **97**, 2194 (1992).
[6] A. Sinha, M. C. Hsiao, and F. F. Crim, J. Chem. Phys. **94**, 4928 (1991).
[7] Y.-H. Chiu, H. Fu, J.-T. Huang, and S. L. Anderson, J. Chem. Phys. **101**, 5410 (1994).
[8] R. D. Guettler, G. C. Jones, Jr., L. A. Posey, and R. N. Zare, Science **266**, 259 (1994).
[9] A. R. Ravishankara and P. H. Wine, J. Chem. Phys. **72**, 25 (1980).
[10] T. N. Truong, D. G. Truhlar, K. K. Baldridge, M. S. Gordon, and R. Steckler, J. Chem. Phys. **90**, 7137 (1989).
[11] W. R. Simpson, A. J. Orr-Ewing, and R. N. Zare, Chem. Phys. Lett. **212**, 163 (1993).
[12] D. F. Varley and P. J. Dagdigian, J. Phys. Chem. **99**, 9843 (1995).
[13] K. D. Dobbs and D. A. Dixon, J. Phys. Chem. **98**, 12584 (1994).
[14] P. Andresen and A. C. Luntz, J. Chem. Phys. **72**, 5842 (1980).
[15] A. C. Luntz and P. Andresen, J. Chem. Phys. **71**, 5851 (1980).
[16] J. Park, Y. Lee, J. F. Hershberger, J. M. Hossenlopp, and G. W. Flynn, J. Am. Chem. Soc. **114**, 58 (1992).
[17] Y.-F. Yen, Z. Wang, B. Xue, and B. Koeplitz, J. Phys. Chem. **98**, 4 (1994).
[18] D. Bogan and D. W. Setzer, ACS Symposium Series **66**, 237 (1978).
[19] D. H. Parker, K. K. Chakravorty, and R. B. Bernstein, J. Phys. Chem. **85**, 466 (1981).
[20] H.-J. Loesch and A. Remscheid, J. Chem. Phys. **93**, 4779 (1990).
[21] B. Friedrich and D. R. Herschbach, Nature (London) **353**, 412 (1991).
[22] H.-J. Loesch and J. Moller, J. Chem. Phys. **97**, 9016 (1992).
[23] H.-J. Loesch and F. Steinkemeier, J. Chem. Phys. **98**, 9570 (1993).
[24] H.-J. Loesch and F. Steinkemeier, J. Chem. Phys. **100**, 740 (1994).
[25] H.-J. Loesch and F. Steinkemeier, J. Chem. Phys. **100**, 4308 (1994).
[26] P. R. Brooks, Science **193**, 11 (1976).
[27] R. Zhang, D. J. Rakestraw, K. G. McKendrick, and R. N. Zare, J. Chem. Phys. **89**, 6283 (1988).
[28] O. Dobis and S. W. Benson, Int. J. Chem. Kinet. **19**, 691 (1987).
[29] R. Atkinson, D. L. Baulch, R. A. Cox, R. F. Hampson, Jr., J. A. Kerr, and J. Troe, J. Phys. Chem. Ref. Data **21**, 1125 (1992).
[30] G. E. Busch, R. T. Mahoney, R. I. Morse, and K. R. Wilson, J. Chem. Phys. **51**, 449 (1969).
[31] Y. Matsumi, K. Tonokura, and M. Kawasaki, J. Chem. Phys. **97**, 1065 (1992).

[32] G. Herzberg, *Infrared and Raman Spectra of Polyatomic Molecules* (Van Nostrand, Toronto, 1966), Vol. 2.
[33] J. K. Wilmhurst and H. J. Bernstein, Can. J. Chem. **35**, 226 (1957).
[34] W. L. Barnes, J. Susskind, R. H. Hunt, and E. K. Plyler, J. Chem. Phys. **56**, 5160 (1972).
[35] W. W. Wiley and I. H. McLaren, Rev. Sci. Instrum. **26**, 1150 (1955).
[36] S. Arepalli, N. Presser, D. Robie, and R. J. Gordon, Chem. Phys. Lett. **118**, 88 (1985).
[37] Y. Xie, P. T. A. Reilly, S. Chilukuri, and R. Gordon, J. Chem. Phys. **95**, 854 (1991).
[38] D. S. Green, G. A. Bickel, and S. C. Wallace, J. Mol. Spectrosc. **150**, 303 (1991).
[39] D. S. Green, G. A. Bickel, and S. C. Wallace, J. Mol. Spectrosc. **150**, 354 (1991).
[40] D. S. Green, G. A. Bickel, and S. C. Wallace, J. Mol. Spectrosc. **150**, 388 (1991).
[41] E. A. Rohlfing, D. W. Chandler, and D. H. Parker, J. Chem. Phys. **87**, 5229 (1987).
[42] W. R. Simpson, T. P. Rakitzis, S. A. Kandel, T. Lev-On, and R. N. Zare, J. Phys. Chem. (submitted).
[43] S. Sakei, M. Mizuno, and S. Kondo, Spectrochim. Acta, A **32**, 403 (1976).
[44] A. J. Orr-Ewing, W. R. Simpson, T. P. Rakitzis, S. A. Kandel, and R. N. Zare, J. Chem. Phys. (in preparation).
[45] Because of a slight geometric misalignment, the photodissociation polarization data were recorded at 8° and 98° from the flight axis. This misalignment was taken into account by the data analysis program and caused only a slight decrease ($\approx$10%) in the sensitivity to the spatial anisotropy of the reactive product.
[46] R. N. Zare, Ber. Bunsenges. **86**, 422 (1982).
[47] A. J. Orr-Ewing and R. N. Zare, in *Chemical Dynamics and Kinetics of Small Radicals*, edited by A. Wagner and K. Liu (World Scientific, Singapore, 1995).
[48] A. J. Orr-Ewing, W. R. Simpson, T. P. Rakitzis, and R. N. Zare, Isr. J. Chem. **34**, 95 (1994).
[49] S. C. Wofsy, J. S. Muenter, and W. Klemperer, J. Chem. Phys. **33**, 4005 (1970).
[50] R. N. Zare, *Angular Momentum, Understanding Spatial Aspects in Chemistry and Physics* (Wiley-Interscience, New York, 1988).
[51] W. H. Press, B. P. Flannery, S. A. Teukolsky, and W. T. Vetterling, *Numerical Recipies* (Cambridge University, Cambridge, 1986).
[52] G. Millot, J. Hetzler, B. Foy, and J. I. Steinfeld, J. Chem. Phys. **88**, 6742 (1988).
[53] J. R. Hetzler and J. I. Steinfeld, J. Chem. Phys. **92**, 7135 (1990).
[54] These cases in which we assume the effect to be caused solely by rotational alignment or vibrational amplitude alignment are the limiting cases of the real effect, that is, the reactivity arising from both vibration and rotation. This correlated reactivity possibly has a changed rotational dependence as a function of vibrational alignment, greatly complicating the deconvolution. With these complicating factors in mind, we note that the simple model of vibrational dependence alone is consistent with the data within error bars, and this model is justified.
[55] J. T. Hougen, in *Physical Chemistry Series Two*, edited by D. A. Ramsay (Butterworths, Boston, 1976), Vol. 3, p. 75.
[56] J. Moret-Bailly, J. Mol. Spectrosc. **15**, 344 (1965).
[57] R. W. Randall, J. B. Ibbotson, and B. J. Howard, J. Chem. Phys. **100**, 7042 (1994).
[58] T. Suzuki and E. Hirota, J. Chem. Phys. **98**, 2387 (1993).
[59] M. Ben-Nun, M. Brouard, J. P. Simons, and R. D. Levine, Chem. Phys. Lett. **210**, 423 (1993).
[60] R. G. Bray and R. M. Hochstrasser, Mol. Phys. **31**, 1199 (1976).
[61] Y. Huang, Y.-A. Yang, G.-X. He, and R. J. Gordon, J. Chem. Phys. **99**, 2752 (1993).
[62] R. Parson, J. Chem. Phys. **93**, 8731 (1990).
[63] R. Parson, J. Chem. Phys. **95**, 8941 (1991).
[64] W. J. van der Zande, R. Zhang, R. N. Zare, K. G. McKendrick, and J. J. Valentini, J. Phys. Chem. **96**, 8205 (1991).